Investigation of Nonhydrolyzable ATP Analogues and Cofilin-Derived Peptides for Inhibition of Cofilin-Actin Rod Formation

By

Collin Townsend O'Bryant

July, 2021

Director of Thesis: Dr. Robert Murray Hughes

Major Department: Chemistry

Abstract

Actin-Cofilin rods are an important marker of neurodegenerative disease and are commonly observed in the neurons of patients with Alzheimer's disease. The goal of this research is to investigate peptide and small-molecules for their potential to inhibit actin-cofilin rod formation in cells. These inhibitors could form the basis for new Alzheimer's disease therapeutics. Using fluorescence microscopy and an optogenetic system known as CofActor in both the HeLa and HEK 293T cell lines, we assessed changes in actin/ cofilin dynamics under energetic stress conditions in the presence of small molecules and cofilin mimicking peptides. Our small molecule strategy uses nonhydrolyzable ATP analogues to block the formation of actin-cofilin rods in cells undergoing energetic stress. Our peptide-based strategy uses cofilin-1, a primary binding protein to F-actin in neurons, as a template for the creation of peptides that target known cofilin-binding sites on the surface of actin. In our small molecule inhibitor strategy, we observed that ATP α-Sulfur analogue was the most promising actin-cofilin rod inhibitor of the compounds tested. We hypothesize that this compound inhibits actin-cofilin rod formation by binding to P2X and P2Y cell surface receptors. In our peptide inhibition strategy, we discovered three peptides that inhibit actin-cofilin rod formation in cells undergoing energetic stress. These peptides were found to

significantly decrease the length of native actin-cofilin rods in stressed cells. In some cases, we observed inhibition of CofActor-induced cofilin-actin clusters in cells under energetic stress. We hypothesize that these peptide-based inhibitors function by binding directly to actin and blocking actin/cofilin interactions. These studies lay the foundation for future work, including incorporating our peptides into optogenetic cassettes to enable light-activated recruitment of proteins to actin and for advanced pharmacological evaluation of ATP α-Sulfur analogues as therapeutics for neurodegenerative disease.

Investigation of Nonhydrolyzable ATP Analogues and Cofilin-Derived Peptides for

Inhibition of Cofilin-Actin Rod Formation

A Thesis

Presented To the Faculty of the Department of Chemistry

East Carolina University

In Partial Fulfillment of the Requirements for the Degree

Masters of Science in Chemistry

By

Collin Townsend O'Bryant

July, 2021

Signature Page

Investigation of Nonhydrolyzable ATP Analogues and Cofilin-Derived Peptides for Inhibition of
Cofilin-Actin Rod Formation

By

Collin Townsend O'Bryant

APPROVED BY:

Director of Thesis or Dissertation   _____

Robert Hughes, PhD

Committee Member   _____

Anne Spuches, PhD

Committee Member   _____

Anthony Kennedy, PhD

Committee Member   _____

Alexander Murashov, MD, PhD

Chair of the Department of Name   _____

Andrew Morehead, PhD

Dean of the Graduate School   _____

Paul J. Gemperline, PhD

Acknowledgement Page

I would like to thank all my friend and colleagues in the graduate chemistry program for making

this such an enjoyable experience. A special thanks to Dr. Robert Hughes for mentoring and

teaching me so much during the process.

Table of Contents

List of Tables

List of Figures

List of Abbreviations

AD - Alzheimer's disease

ATP - Adenosine triphosphate

ADP - Adenosine diphosphate

AMP - Adenosine monophosphate

HeLa - Henrietta Lacks

HEK 293T - Human embryonic kidney 293 T-antigen

Cry2 - Cryptochrome 2

CIB1 - Cryptochrome-interacting basic-helix-loop-helix

CIBN - Cryptochrome-interacting basic-helix-loop-helix

PHYB - Phytochrome B

hr - Hour/s

nm - nanometer/s

μm - micrometer/s

μM - micromolar

mM - millimolar

LOV - Light-oxygen-voltage

PAS - Per-Arnt-Sim

Aβ - amyloid beta

Ab - Antibody

APP - amyloid precursor protein

ApoE4 - Apolipoprotein E

CaN - Calcineurin

GSK-3 - Glycogen synthase kinase-3

PAK - Serine/threonine-protein kinase

NMDAR - Anti–N-Methyl-D-Aspartate Receptor

AMDAR - α-amino-3-hydroxy-5-methyl-4-isoxazolepropionic acid receptor

PSD - Postsynaptic density

GFP - Green Florescent Protein

REDOX - reduction–oxidation

ENPP - ectonucleotide pyrophosphatase/phosphodiesterase

Ca^{2+} - Calcium Ion

P2X - Adenine Nucleotide Activated Purinoceptor

P2Y - Adenine Nucleotide Activated Purinoceptor

ROS - Reactive oxygen species

E-NTPDase - Ecto-5'-nucleotidase

A_x - Purinoceptor activated only by adenosine

PBS - Phosphate-buffered saline

PDB - Protein Data Bank

DPBS - Aliquots of Dulbecco's PBS with calcium and magnesium

DDG - 2-Deoxy-d-glucose

PFA - paraformaldehyde

CST Ab dilution buffer - Cell Signaling Technology Antibody dilution buffer

Avg - average

DNA - Deoxyribonucleic acid

DAPI - 4′,6-diamidino-2-phenylindole blue florescent DNA stain

Expt – experiment

PCR - Polymerase Chain Reaction

SOC - Super Optimal broth

FRAP - Fluorescence recovery after photobleaching

STORM - Stochastic Optical Reconstruction Microscopy

Chapter 1:   Introduction

Alzheimer's disease (AD) is a major cause of age-related dementia affecting millions of people that, as of now, has no currently approved treatment for the causes of the dementia.[1,2] AD is a major condition that has plagued the population is preparing to become one of the leading age-related causes of death in the next few decades. Dementia, the acquired progressive cognitive impairment sufficient to impact activities of daily living, is a major cause of dependence, disability and mortality.[3] Current estimates says that around 44 million people live with dementia worldwide where this is expected to more than triple by 2050 as the elderly population grows.[3] AD is the single biggest cause of dementia, accounting for 50%–75% of all cases.[4] Most persistent in later years of life, it roughly doubles in prevalence every 5 years after the age of 65.[5] As the population of elderly people grows, we will more than likely encounter a drastic increase in the number of Alzheimer's cases within the next few decades. This will require a major improvement in AD therapies within the near future. The relationship between the major contributors of AD such as amyloid deposits, neurofibrillary tangles and cell death and cognitive impairment remains a mystery.[2] As a result, scientists have been studying the mechanisms behind cognitive impairment in AD. However, studies to prevent these cognitive decay mechanisms in AD patient's cells has not been thoroughly explored. One of which is a known correlation between AD patient's cells exhibiting small rod like structures comprised of a cofilin-saturated actin filament that is being prevented from being depolymerized, causing cell stress and eventual apoptosis.[6]

In this research, I have used optogenetic techniques to stimulate actin-cofilin protein clusters under stress conditions similar to those found in AD neurons undergoing energetic stress and have investigated possible strategies for their inhibition. In one strategy, I have investigated the potential of nonhydrolyzable ATP analogues for the inhibition of cytoskeletal abnormalities

observed under energetic stress. In a second strategy, I have investigated peptides derived from known human cofilin-1 actin G- and F-binding sites as potential inhibitors of cytoskeleton dysregulation in cells undergoing energetic stress. The goal of this study is to identify small molecules and peptides that could be developed into therapies for the reduction or elimination of actin-cofilin rods in energetically stressed cells such as those found in patients with AD. To achieve this goal, I implemented these small molecules and peptides into HeLa and HEK-293T cell models under induced energetic stress levels to observe mechanisms commonly found in neurons of AD patients.

Chapter 2:   Literature Review

Optogenetics is a relatively new technique in neuroscience that allows for light sensitive proteins to observe and control cell mechanisms through both actuators and sensors.[7] The human brain and central nervous system is incredibly complex and even now our understanding of neural activity and communication is limited.[8] Optogenetics, as the name implies, is a combination between light and genetics. This combination allows us to study the complex signaling that occurs in our neurons at the same speed as the signals being sent. This technology was originally theorized to help understand the complexity of the brain by allowing us to use light to activate or inhibit specific neurons in the brain.[9] The first optogenetic methods used rhodopsin-like photosensitive ion channels to stimulate neuronal activity. Opening of ion channels leads to an influx of ions into the cell, which causes a change in the electric potential across the membrane. Depending on what type of channel was effected, you could see an increase or decrease of associated neuronal activities.[9] The development of the second generation of optogenetic modules were based on photoreceptor protein domains that underwent light-induced dimerization/oligomerization or unfolding upon light activation (photo-uncaging).[9] This is the main idea for the work in this paper as the "second generation" has much more potential as a biochemical tool. There are many different models that have been engineered today that have been derived from many different plant and animal proteins. For example, Cryptochrome 2 or CRY2 is a blue-light photoreceptor class from Arabidopsis thaliana belonging to the cryptochrome protein family. It is present in most animals and binds flavin adenine dinucleotide as a co-factor. Upon blue-light exposure, CRY2 undergoes photoisomerization and binds to the N-terminal domain of Cryptochrome-interacting basic-helix-loop-helix (CIB1), more commonly referred to as CIBN. The activation wavelength is 450 nm and the dissociation time of the complex is about 5 min, making this system suitable for

most *in vivo* applications.[9,10] This CRY2/ CIBN complex is the specific system that was used in the research from this paper. Another example is the Phytochrome B (PHYB) photoreceptor which belongs to the phyotochrome protein family and can be found in plants and bacteria. PHYB has a unique feature of being sensitive to red and far-red light. PHYB can be activated with 650 nm red light. However, the dissociation of the dimer in the dark is very slow (~20 hr), but it can be instantaneously triggered by 740 nm far-red light, which makes this system ideally suited for applications requiring fast on/off control of protein activity.[9] All optogenetic systems share similar mechanisms which include localization, clustering, sequestering, and photo-uncaging, all of which are illustrated in **Figure 1**.
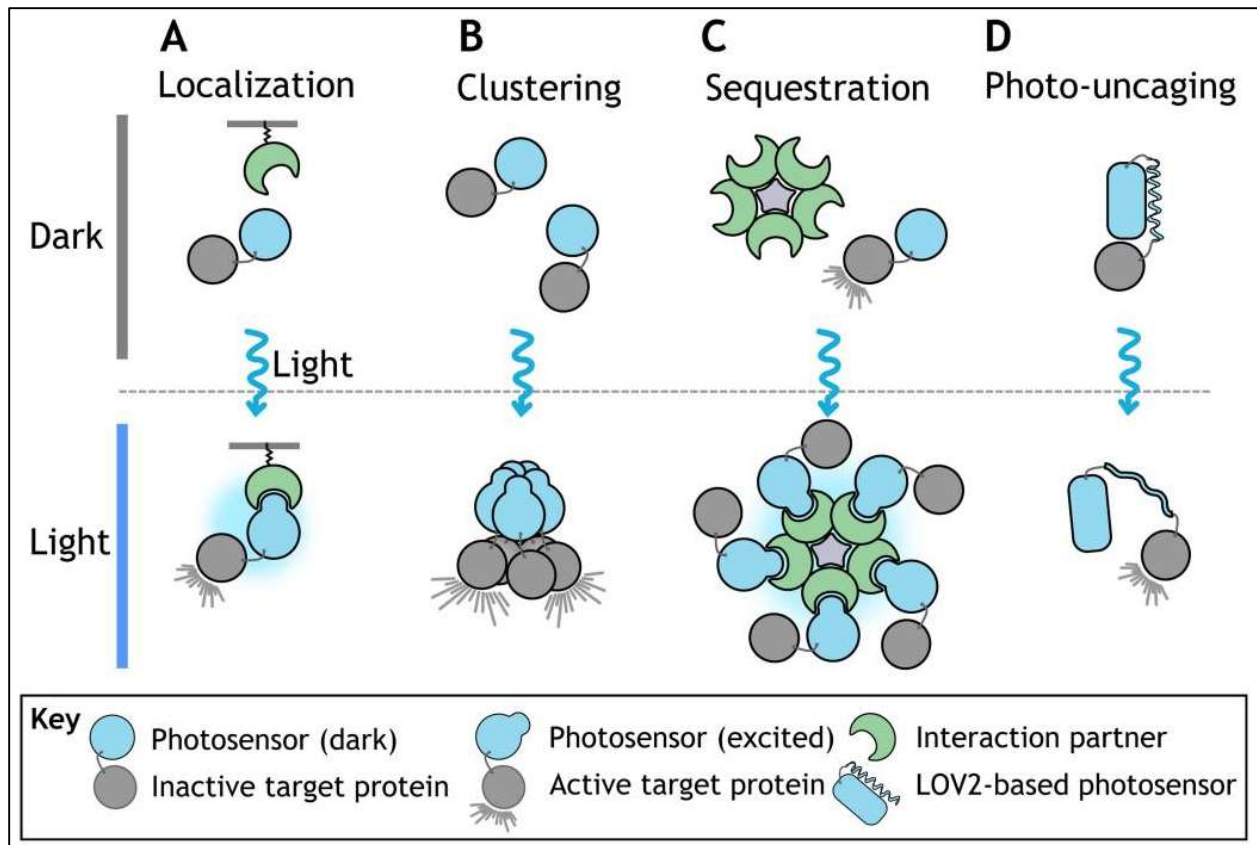
Figure 1: Optogenetic Systems Diagram
(A) Light-induced protein dimerization can be used to recruit a protein of interest to a specific intracellular location, where it can pursue its function. (B) Light-dependent oligomerization (clustering) can induce active functional signaling hubs or inhibit protein function. (C) Light-induced dimerization can also be adopted to sequester a protein of interest away from its site of action. (D) Photo-uncaging based on LOV domains can be used to directly control protein activity with light. (Figure from Krueger, et. Al. 2019)[9]

Light-oxygen-voltage (LOV) domains undergo a unique change known as photo-uncaging. The LOV core domain is composed of a conserved Per-Arnt-Sim (PAS) domain, which is ~110 amino acids long and forms a five-stranded antiparallel β-sheet fold and α-helical connector. Upon blue-light excitation, a covalent bond forms between a cysteine in the PAS domain and flavin (adduct formation), which leads to a conformational change and unfolding of one of the α-helices as seen in **Figure 1-D**.[9] Optogenetics techniques have an advantage when investigating the complex nature of neural pathways as it can bring to light some of the key functions that are damaged from neural

degeneration from diseases like AD. Optogenetic interactions can match the speed of electrical neuronal activities making it easy to use time based experimental intervals and environments for repeat experiments.[7] With the flexibility of optogenetic techniques, we can observe different neuronal activities under stressed cells similar to those from patients with AD.

One of the major theories of AD is the amyloid hypothesis.[11,12] This states that the accumulation of pathological forms of amyloid beta (Aβ) produced by segmentation of the amyloid precursor proteins (APP) by the β- and γ-secretase enzymes in the brain is the primary pathological process, driven through an imbalance between Aβ production and Aβ clearance.[3,12,13] Strong support for a central role for Aβ also comes from genetics. All familial AD mutations are involved in either Aβ generation or processing and result in relative overproduction of toxic forms of Aβ.[3] Once thought to be amyloid plaques, in recent years, the attention has switched to soluble Aβ oligomers as being the most dangerous in terms of its most destructive form.[14] Aβ oligomers purified from AD brains and applied to neurons *in vitro* inhibit long-term potentiation which leads to synaptic dysfunction, damages dendritic spines and causes neuronal death.[3] This means that the amyloid plaques that we have observed may be a necessary catalyst for the supply of the free and soluble oligomers that can lead to downstream induction of tau hyperphosphorylation and neural toxicity. Microtubule associated protein tau is a phosphoprotein which potentially has 80 serine/threonine and 5 tyrosine phosphorylation sites. Normal brain tau contains 2-3 moles of phosphate per mole of the protein. In AD brain, tau is abnormally hyperphosphorylated to a stoichiometry of at least three-fold greater than normal tau, and in this altered state it is aggregated into paired helical filaments forming neurofibrillary tangles, a staple characteristic of the disease.[15–17] An overview of the proposed pathogenesis of AD through the amyloid theory is presented in **Figure 2**.
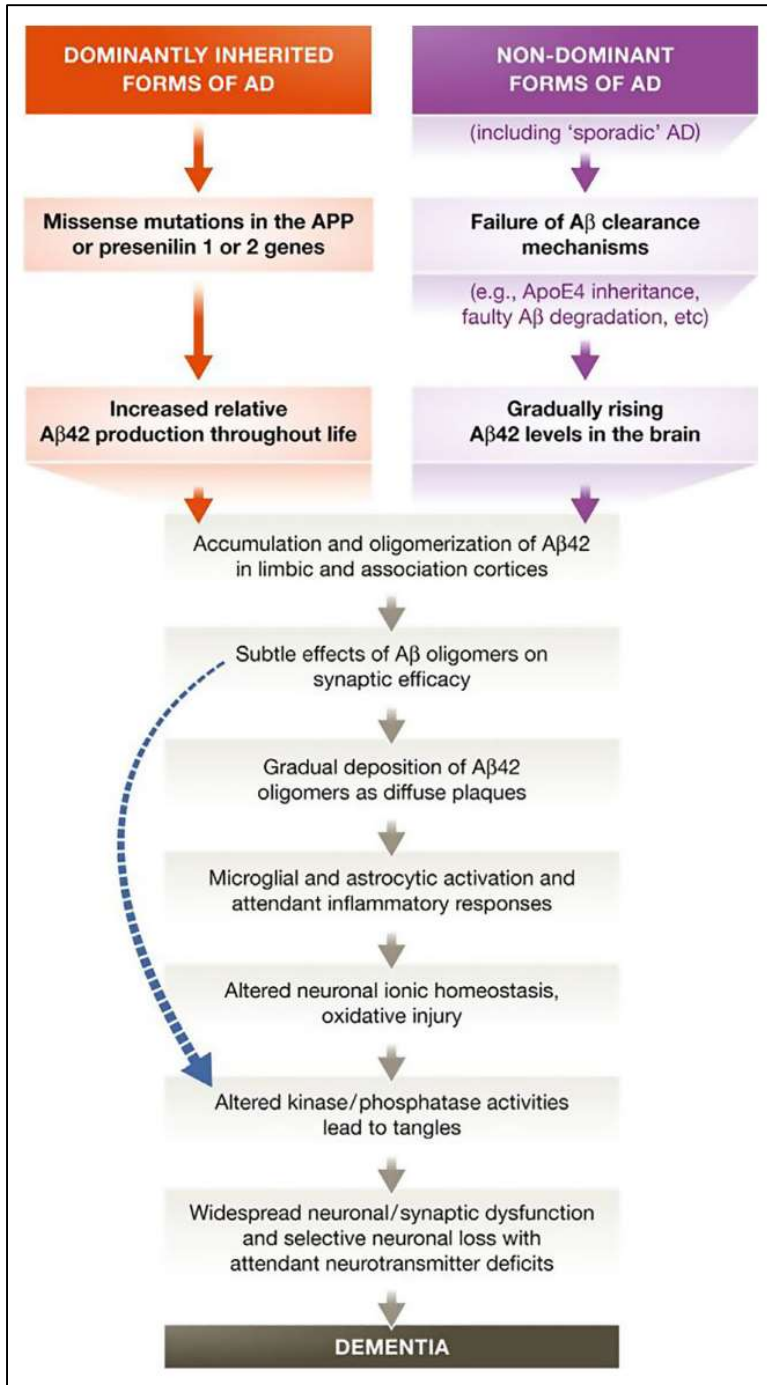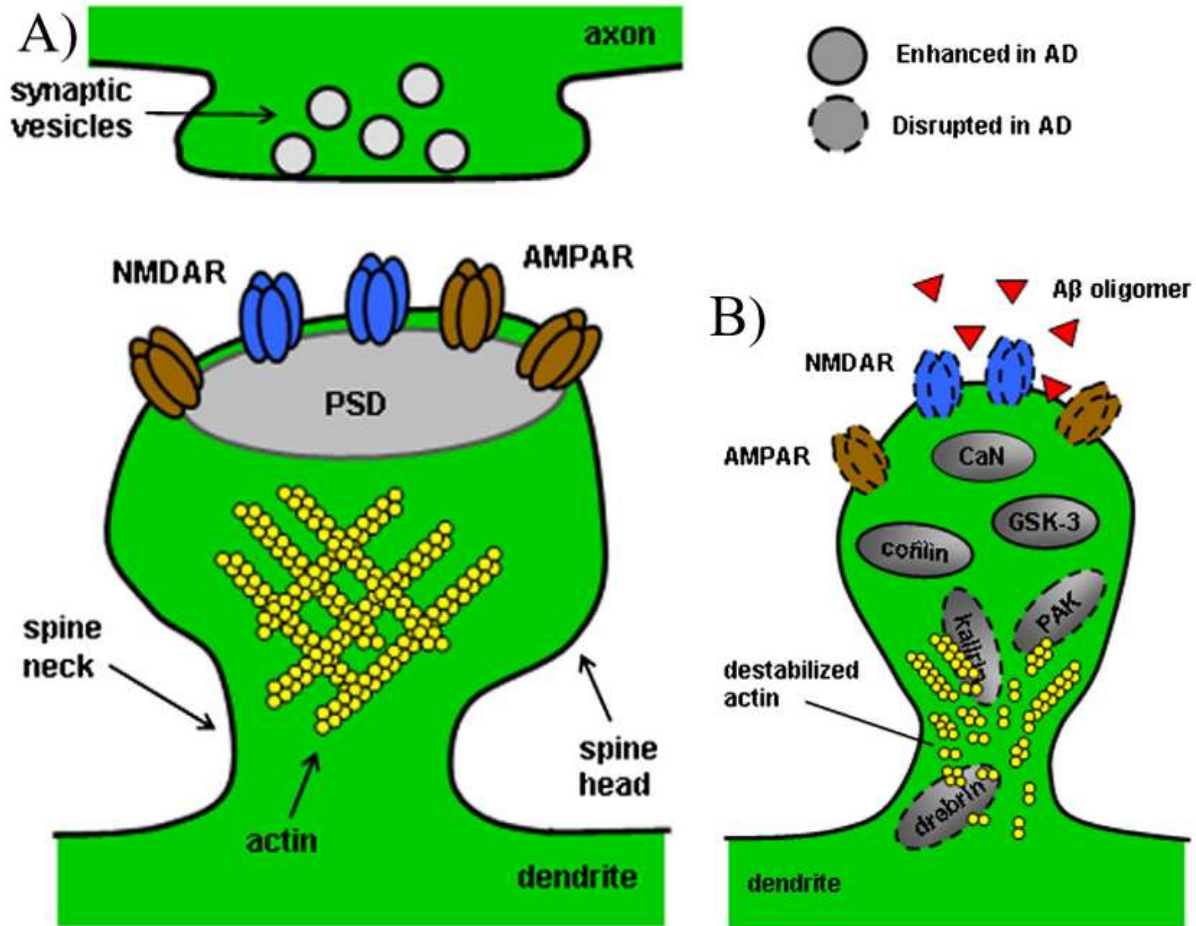
Figure 2: Alzheimer's Disease Progression through Amyloid Hypothesis
An overview of the pathogenesis leading to AD as proposed by the amyloid hypothesis. The curved blue arrow indicates that Aβ oligomers may directly cause synaptic and neuronal damage and induce tau hyperphosphorylation, in addition to activating damaging inflammatory cascades. (Figure from Lane, et. Al. 2018)[3]

One of the major debilitating conditions that are present in neurons of AD patients is a degradation of synapses. During the normal process of aging, our neuronal loss is at a minimum as compared to people with neurodegenerative diseases, with the hippocampal neurons remaining completely unaffected. However, with patients with AD, up to 50% of widespread synaptic loss occurs with selective, localized neuron loss.[18] Overexpression of normal proteins or accumulation of abnormal proteins have been shown to bring about this neurodegeneration.[18] Recent studies suggest that actin-cofilin rods can lead to synaptic toxicity.[19] This synaptic toxicity indicates a correlation between actin-cofilin rod formation and cognitive impairment.[20] Because of this cytoskeletal dysregulation of actin, the signal interactions between the dendrite and the synaptic vesicles are disrupted, causing an irreversible loss of cytoskeletal strength and synaptic response.[21] Actin is a structural protein in all cells which has many influences on the cell's motility, structural rigidity, transport, and membrane interactions. However, actin has shown to have many ways of interacting with other protein structures during assembly. Abnormalities in actin and its cellular interactions can cause drastic changes in the nature of the actin filaments resulting in a disruption in the structure of the filaments or lead actin-cofilin rod formation.[18] Similar to the diagram shown in **Figure 3** below, synaptic degradation occurs because of the overexpression of some proteins such as cofilin (an actin-binding regulator protein), Calcineurin (CaN; a Ca^{2+} channel regulator) and Glycogen synthase kinase-3 (GSK-3) where normally the regulation of actin stability would be monitored by other proteins such as drebrin (an actin regulating protein within neurons specifically), Serine/threonine-protein kinase (PAK) and kalirin (plays a role in synaptic plasticity) which are disrupted in AD making actin structures unstable.[2]

Figure 3: Decay of synapses in Alzheimer's Disease
Synaptic actin cytoskeleton destabilization in AD through overexpression of actin intrusion proteins and disruption of actin stabilizing proteins. A) healthy synapses, B) Decay of synapses in AD. (Figure from Penzes, et. Al. 2011)[2]

There have been studies that support the interactions between actin and these actin regulating proteins, specifically cofilin, as it functions as an actin regulator within the cells.[1,2,22] In the presence of ATP, actin will polymerize into a semi-immobilized state where the stability of this state is described as the critical concentration for polymerization. The Critical concentration of polymerization is described as the concentration of free monomers in equilibrium with the filaments.[22] This is known as actin "treadmilling" and is shown in **Figure 4**.
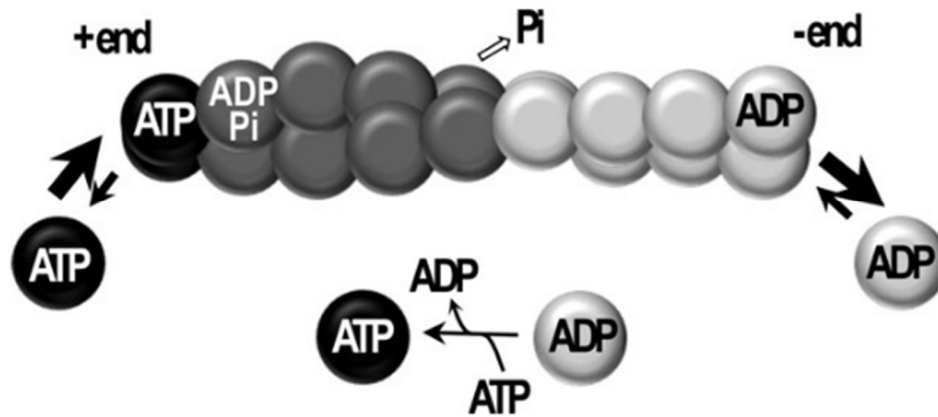
Figure 4: Actin Treadmilling
Hydrolyzing ATP to ADP within the actin structure then releasing the ADP back into the system at the less stable (-) end of the filament. ATP is hydrolyzed to ADP and cycled back to form a stable "treadmill" effect. (Figure from Kudryashov, et. Al. 2013)[22]

Cofilin interacts with the ADP actin state to promote depolymerization from the barbed end (-) to recycle actin monomers back into the cell.[23,24] This treadmilling effect is destabilized in patients with AD and can be influenced by the intrusion proteins listed above giving rise to actin-cofilin rod formation and the consumption of ATP without the ADP recycling.[2,22]

Chapter 3:   Research Questions

One of the main concerns in AD research is the lack of preventative measures against cognitive decline. Once the synapses and neurons have been affected by the disease, the damage that they suffer is irreversible. The goal of my research is to answer whether I can use small molecule inhibitors or mimicking peptide chains to inhibit the formation of actin-cofilin rods which have been common physical aspects in AD patient's neurons. This inhibition could lessen the impact on the synapses and prevent the permanent damage that occurs after prolonged stressed conditions. To investigate this, I will use optogenetic techniques to observe inhibition of cell mechanisms in the presence of nonhydrolyzable ATP analogues and cofilin mimicking peptide as potential inhibitors within HeLa and HEK-293T cell lines under energetic stress conditions.

As stated previously, actin-cofilin rods are a key factor in the disruption and degradation of neurons in neurodegenerative diseases. In stressed neurons, the actin rod formation occurs in a 1:1 ratio with cofilin in the brains of AD patients. To observe the behavior of the actin-cofilin complex, researchers have developed a light responsive Cry2-CIB switch called "CofActor" that, when exposed to blue light and energetic or oxidative stress, will cluster together. This system can be used to monitor the changes in actin-cofilin interactions when applying the theorized methods for actin-cofilin rod inhibition.[25,26]
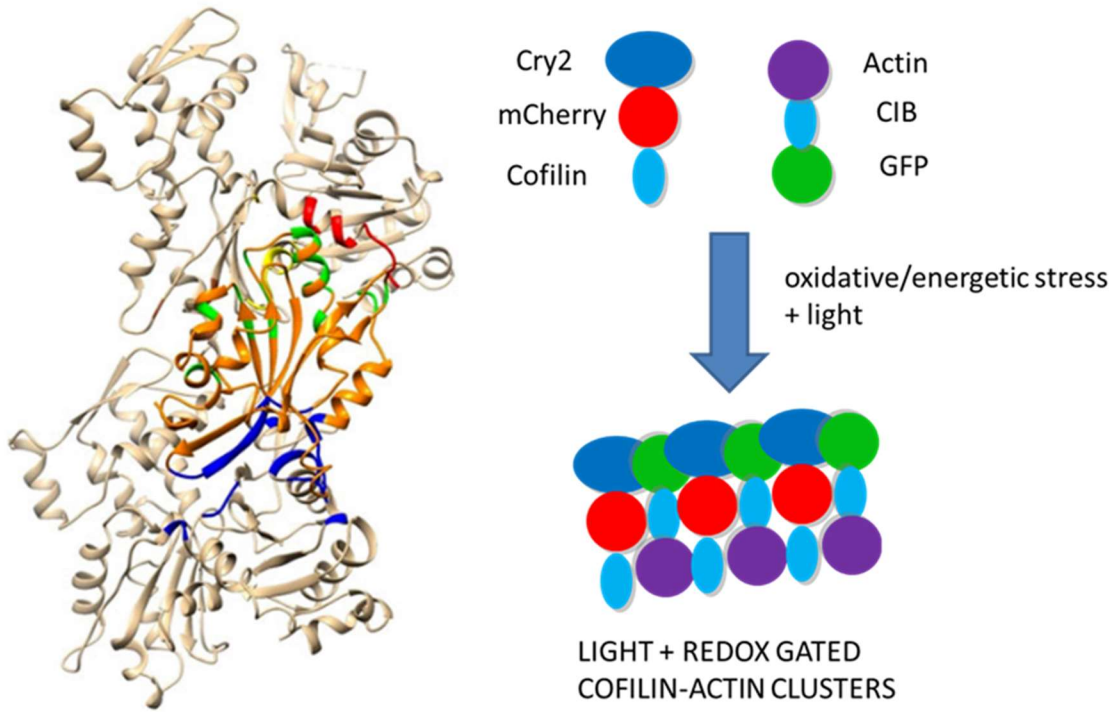
Figure 5: Optogenetic CofActor System
Actin bound to cofilin in a 1:1 ratio. The optogenetic switch used to monitor the changes in actin-cofilin interactions when applying the theorized methods for actin-cofilin rod inhibition (Figure from Tanaka et. Al. 2018).[26]

Chapter 4:   Nonhydrolyzable ATP Analogue Studies

To investigate the possibility of preventing actin cytoskeleton instability, I will attempt to target the ATP-actin treadmilling mechanism. By using nonhydrolyzable ATP analogues, the hypothesis is that it will not allow the construction of the irreversible actin rods that consume normal ATP. Previous research suggests that nonhydrolyzable ATP binds more readily to ATP-actin states than normal ATP.[22,27] The nonhydrolyzable ATP analogues also have a history of being a known inhibitor of ectonucleotide pyrophosphatase/phosphodiesterase (ENPP) which is overexpressed in brain tissue in neurodegenerative diseases and is a major contributor to hydrolyzing phosphodiester and pyrophosphate bonds of nucleotides.[28] Because of their upregulation, the overconsumption of ATP in neurodegenerative diseased cells is even more prevalent leading to a faster progression to irreparable damages. When working with ATP concentrations, it is also important to consider the possibilities of interrupting downstream processes that are ATP dependent. It is known in recent studies that distinct pathways of ATP-gated Ca^{2+} entry via ionotropic purinoceptor subtypes is a crucial contributor to Ca^{2+} signals important for ion channel activation.[29,30] Experimentation has shown that both rodent models and human salivary glands express $P2X_4$ and $P2X_7$ purinoceptors that function as non-selective, Ca^{2+}-conducting cation channels.[29,31,32] These receptors are notably linked to ATP and fluctuations in the intracellular concentrations of ATP. Additionally, Ca^{2+} signals can be generated in salivary gland cells by ATP application which activates the P2X class ion channels via a pathway that is alternative and largely independent of inositol trisphosphate receptor Ca^{2+} production which has been shown to result in an elevation of $[Ca^{2+}]_i$.[29] ATP dysregulation is an important factor that influences oxidative stress within neurons. Oxidative stress is when intracellular generation of reactive oxygen species (ROS) exceeds the cell's ability of both non-enzymatic and enzymatic

anti-oxidation mechanisms.[33] Adenosine and guanosine, along with purinergic receptors are important for neuroprotection and are also involved in regulating the hydrolysis of ATP. The intricate relationship between adenosine nucleotides, ecto-enzymes metabolizing adenosine nucleotides, and purinergic receptors can be seen in **Figure 6** below.
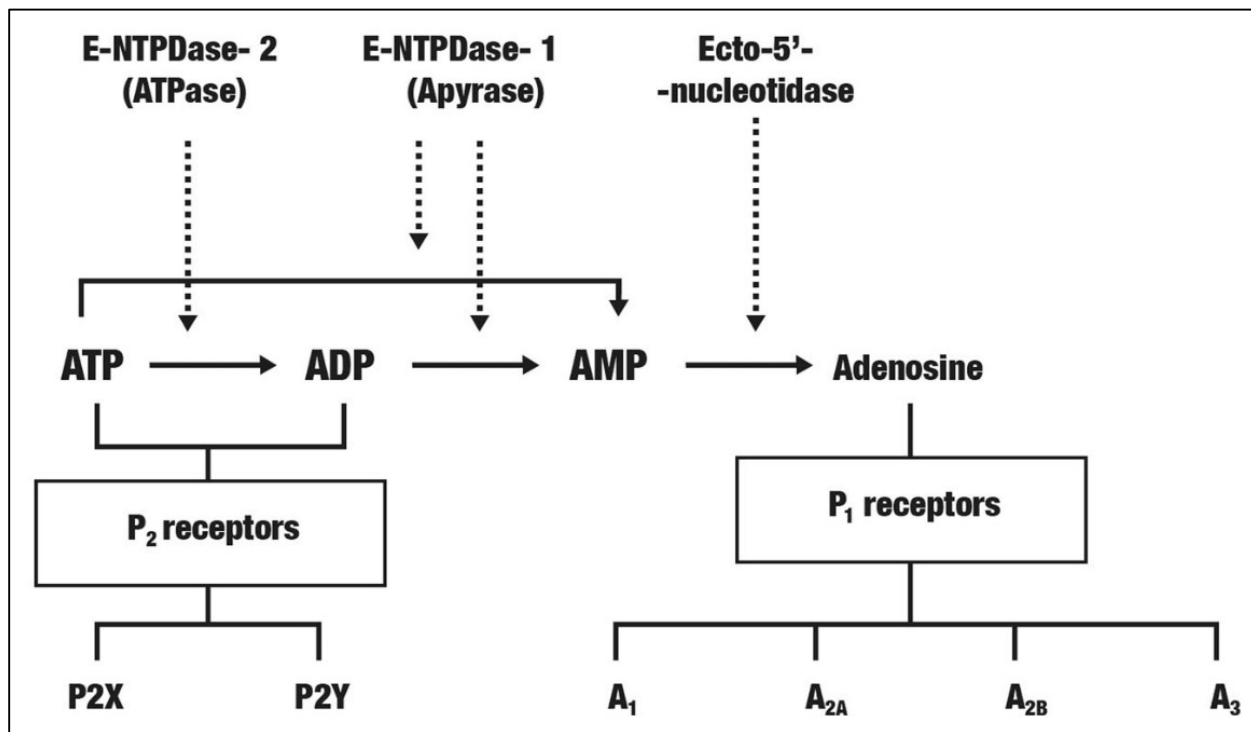
Figure 6: ATP/ ADP and the P2X/ PSY Receptors
Relationships between ecto-enzymes metabolizing adenosine nucleotides, adenosine nucleotides, and purinergic receptors in the central nervous system cells, which are related to the etiology of AD (Figure from Cieślak et. Al. 2018).[33]

In AD, the Aβ peptide causes the formation of ROS, in particular hydrogen peroxide, which is capable of reacting with the metal ions such as calcium present in the senile plaques. Increased levels of Ca^{2+} as also been seen as an unwanted condition that can lead to unintentional cell stress which could be detrimental to this paper's research.

4.1: ATP analogue experiments in HeLa Cell Line

Previous research suggests that nonhydrolyzable ATP analogues bind more readily to ATP-actin states than normal ATP. Our small molecule strategy uses nonhydrolyzable ATP analogues to block the formation of actin-cofilin rods in cells undergoing energetic stress. the initial library of nonhydrolyzable ATP analogues are illustrated in **Figure 7** where the change from native ATP is circled in red.
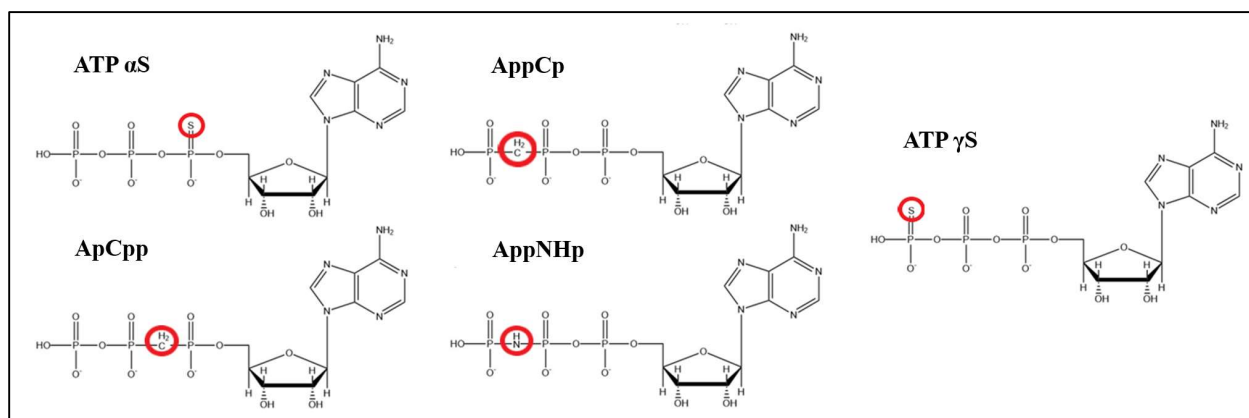
Figure 7: Nonhydrolyzable ATP Analogue Library
Nonhydrolyzable ATP analogues (ATP-αS, ApCpp, AppCp, AppNHp, and ATP-γS; chemicals received from Jena Bioscience) and their changes from native ATP indicated by the red circles in each molecule.

4.1.1: Experimental Design

Using five different nonhydrolyzable ATP analogues (ATP-αS, ApCpp, AppCp, AppNHp, and ATP-γS; chemicals received from Jena Bioscience) an energetic stress protocol was conducted. Once the HeLa cells reached a sufficient concentration, the cells were diluted to ~200,000 cells/mL and transferred to small glass bottom dishes where they were left at 37°C overnight to attach to the dish. Aliquots of Dulbecco's PBS with calcium and magnesium (DPBS, 270 μL) were prepped in 1.5 mL tubes, 30 μL of each ATP analogue was added for a total of 300 μL. The media was aspirated from the HeLa cells and washed with 1 mL of DPBS. The 300 μL

aliquots were added to each set of cells leaving one blank control and one stressed control and incubated for 5 minutes at 37°C. The dish was removed from the incubator and 4.8 μL of the stress inducing solution (30 μL of 1M sodium azide and 18 μL of 1M 2-Deoxy-d-glucose (DDG)) was added to the cells and incubated at 37°C for 15 minutes. The cells were removed from the incubator and washed with 1 mL of DPBS and 1 mL of pre-warmed fixative (37°C; 4% PFA (Electron Microscopy Sciences and DPBS)) and allowed to sit at room temperature for 45 minutes. The fixative was removed, and the cells were washed with DPBS, covered in 1.5 mL of DPBS, wrapped in parafilm and placed in the refrigerator until ready to perform the immunostaining.

For the immunostaining process, the cells were permeabilized for 3 minutes with pre-chilled methanol (-20°C) then blocked for 30 minutes with CST Ab dilution buffer (30 μL Triton X-100, 0.1 g of BSA, and 10 mL of DPBS) and incubated overnight at 4°C with primary antibody (Anti-β-Actin Antibody (C4) mouse monoclonal IgG$_1$ (Santa Cruz)) and 1:500 in Ab dilution buffer. The following day, the primary antibody solution was removed via pipette and washed 3 times with 1 mL of DPBS. The cells were then incubated with Alexa 488 conjugated goat anti-mouse secondary (Invitrogen; 1:200 Ab dilution buffer) for 1 hour at room temperature followed by a wash with DPBS (3 times) and stored in 1.5 mL of DPBS prior to imaging. The images were then taken on a Leica Fluorescence microscope.

To prepare the cells for the optogenetic experiments, HeLa cells were pipetted onto a small glass bottom dish (~200,00 cells/mL). The cells were transfected with a GFP control and then co-transfected with 1000 ng of DNA from both Actin-CIB-GFP and CofilinS3E-Cry2-mCherry using Lipofectamine 3000 and incubated at 37°C overnight. For a 6-well plate size transfection reagent procedure, 125 μL of Opti-MEM and 5 μL of P3000 was added to the DNA. In a separate container, 125 μL of Opti-MEM and 3.75 μL Lipofectamine 3000 reagent per sample were mixed

to make a stock. The reagent stock (~127 μL per sample) was added dropwise to an aliquot of HeLa cells. The DMEM media was aspirated, and the cells were incubated with the ATP analogue solution for 15 minutes prior to cell imaging.

4.1.2:   Results

In this experiment, we observed the formation of cofilin-actin rods in our energetic stress-treated control sample. By contrast, in our non-stress-treated sample, no cofilin-actin rods were observed. Going forward, we continued to observe the changes in the actin dynamics within the cell models with the addition of different concentrations of the ATP analogues. Based on the data gathered, the reactions from the ATP-αS (C) and ATP-γS (G) were the most promising candidates for inhibiting cluster formation during light activation when cells were transfected with the optogenetic proteins. Because they exhibited none or slight evidence of actin-cofilin rod formation and an increased cellular adhesion formation, the sulfur containing analogues were used in optogenetic protein and concentration assay experiments to determine the best concentration and cluster inhibition efficiency.
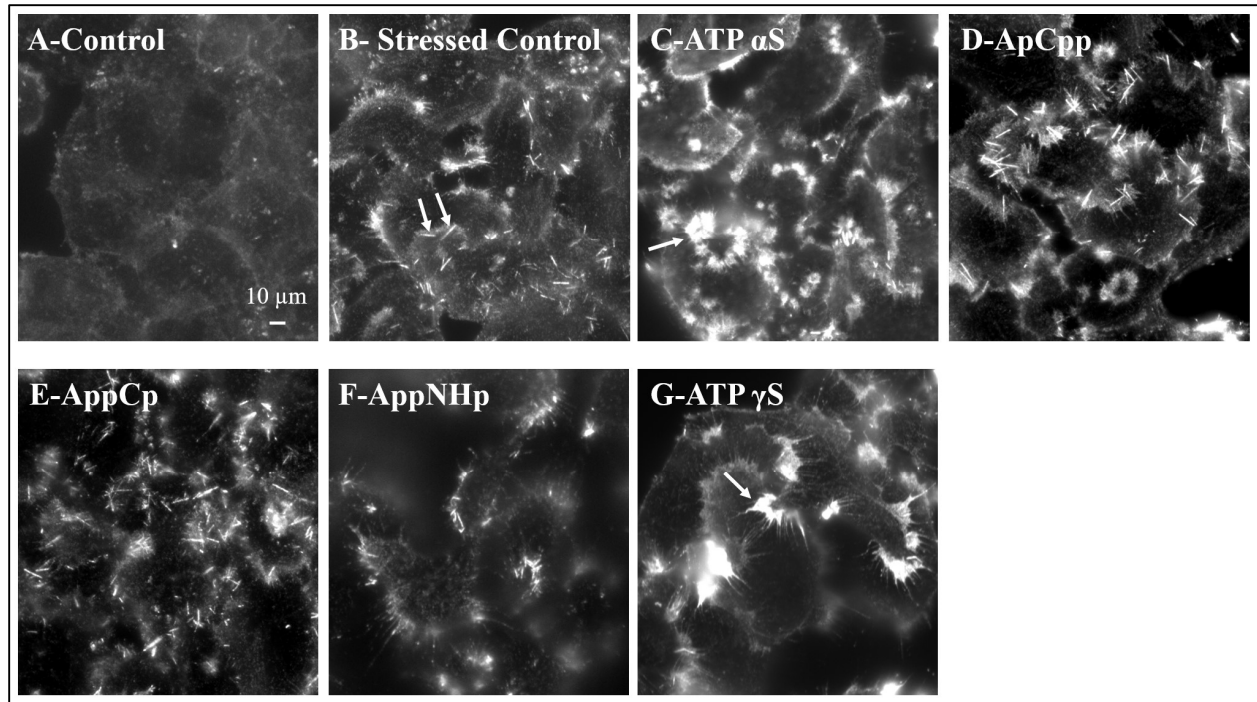
Figure 8: Nonhydrolyzable ATP analogues Native Actin Rod Interaction
Leica microscope images of HeLa cells treated with nonhydrolyzable ATP analogues under energetic stress conditions. White arrows indicate specific actin rods and focal adhesions. (4.8 µL; 0.625 M sodium azide: 0.375 M DDG); (A) Control cells, (B) Oxidant control cells, (C) ATP-α Sulfur treated cells, (D) ApCpp treated cells, (E) AppCp treated cells, (F) AppNHp treated cells, (G) ATP-γ Sulfur treated cells.
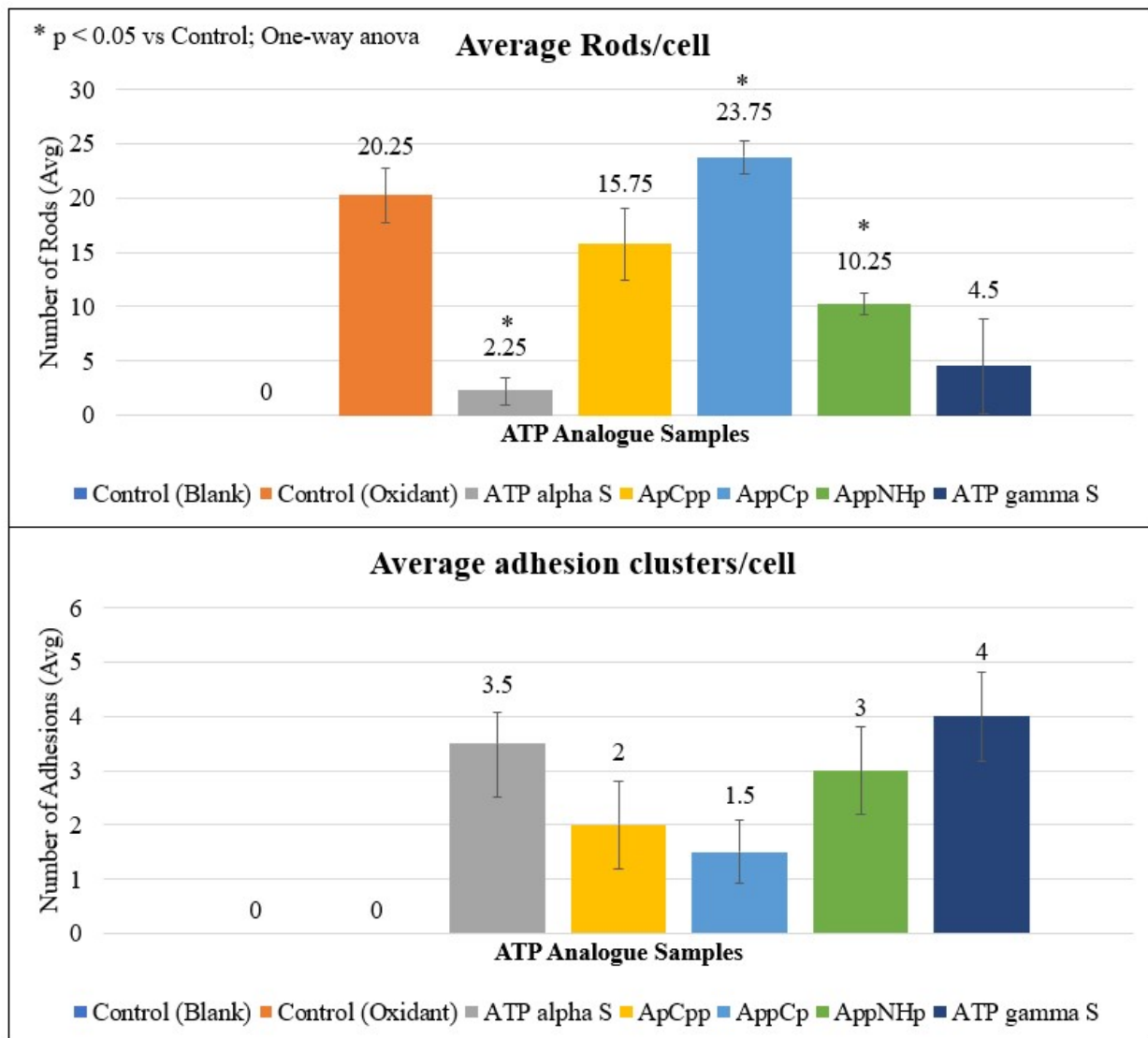
Figure 9: ATP Experiments; Average actin rods (top) and Average focal adhesions (bottom) Bar graphs corresponding to ATP analogues experiments in HeLa cells. Average actin rods and focal adhesions per cell in the sample where n=100 cells for each condition. ATP α Sulfur, AppNHp, and ATP γ Sulfur samples for rods/cell are statistically significant ($p < 0.05$) via a one-way ANOVA compared to the control sample.

I later repeated the native rod formation experiment in HeLa cells with a non-stressed and one-hour stress condition to confirm the results and prepared for the concentration assay which was to investigate the P2X and P2Y receptor theory along with any evidence of concentration dependent actin-cofilin rod inhibition. The results were comparable to the first experiment; however, the images were taken on a Zeiss 700 and 900 Confocal microscopes. With the better

resolution, the effects on the actin filaments and actin-cofilin rods were easily seen. The control, ATP alpha and gamma sulfur images, found below are all under a 1-hour energetic stress condition incubated with the ATP analogues for 15 minutes prior to the addition of the stress solution.
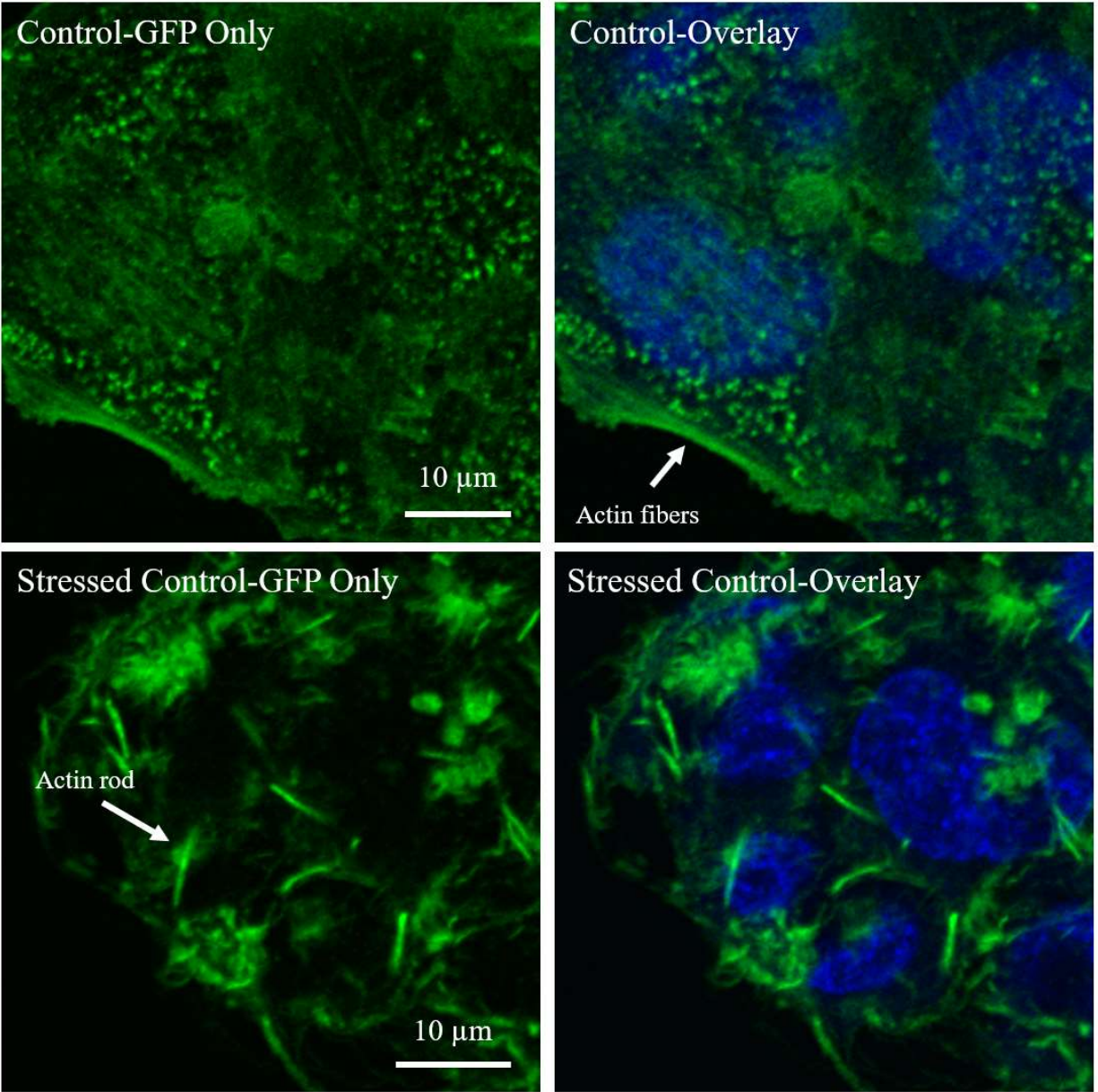
Figure 10: Native ATP Sulfur analogue expt; Control
Zeiss 700 Confocal microscope images; HeLa cells; Control-Non-stressed (top left & right) and Stressed (4.8 µL; 0.625 M sodium azide: 0.375 M DDG), (bottom left & right) with GFP-only vector (Green) and DAPI (Blue)/GFP (Green) overlay.
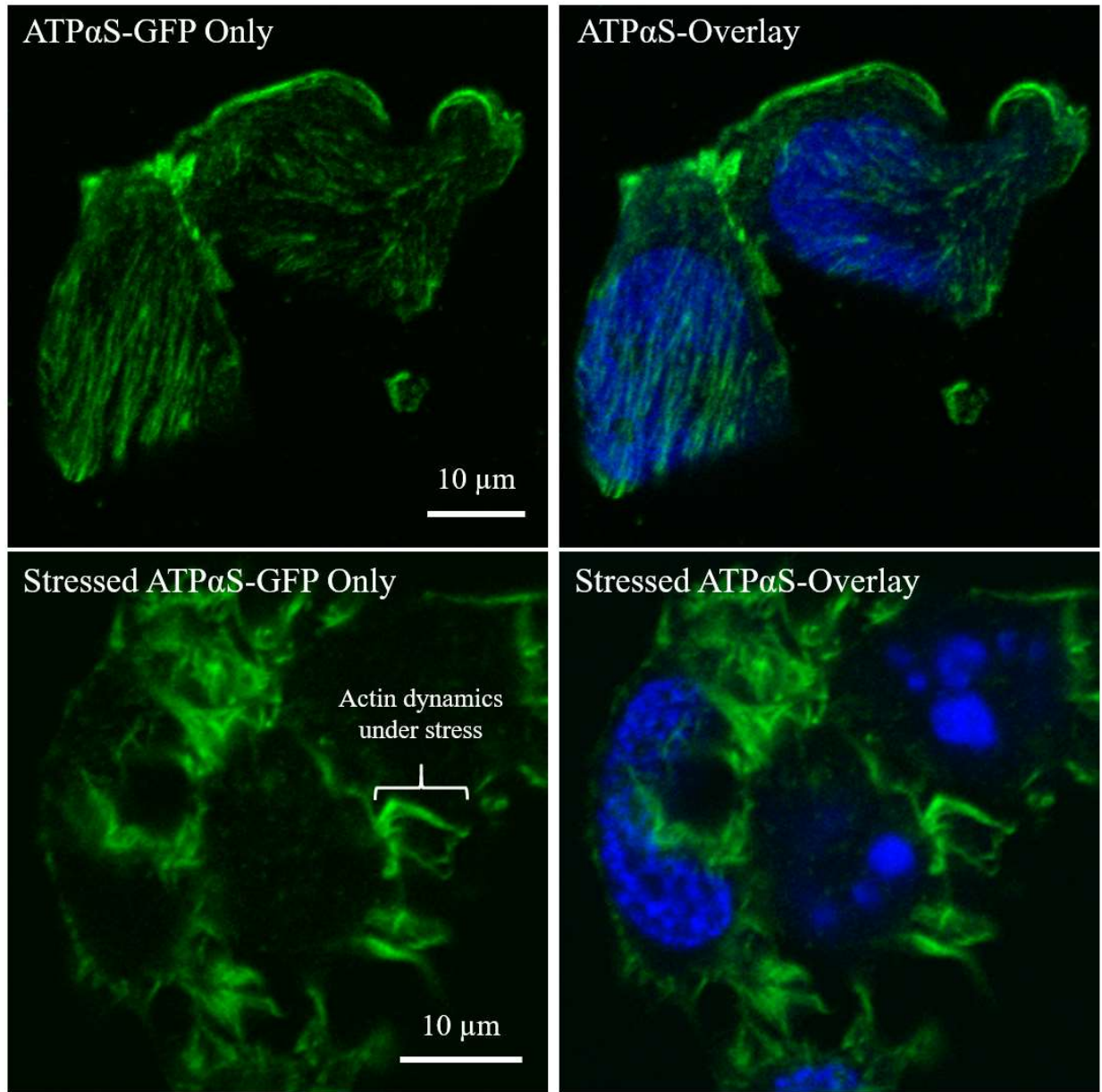
Figure 11: Native ATP Sulfur analogue expt; ATP α-Sulfur (700)
Zeiss 700 Confocal microscope images; HeLa cells; ATPαS-Non-stressed (top left & right) and Stressed (4.8 µL; 0.625 M sodium azide: 0.375 M DDG), (bottom left & right) with GFP-only vector (Green) and DAPI (Blue)/GFP (Green) overlay.

Figure 12: Native ATP Sulfur analogue expt; ATP α-Sulfur (900)
Zeiss 900 Confocal microscope images; HeLa cells; ATPαS-Stressed (4.8 µL; 0.625 M sodium azide: 0.375 M DDG) only with GFP-only (Green, left) and DAPI (Blue)/GFP (Green) overlay (right).

Figure 13: Native ATP Sulfur analogue expt; ATP γ-Sulfur
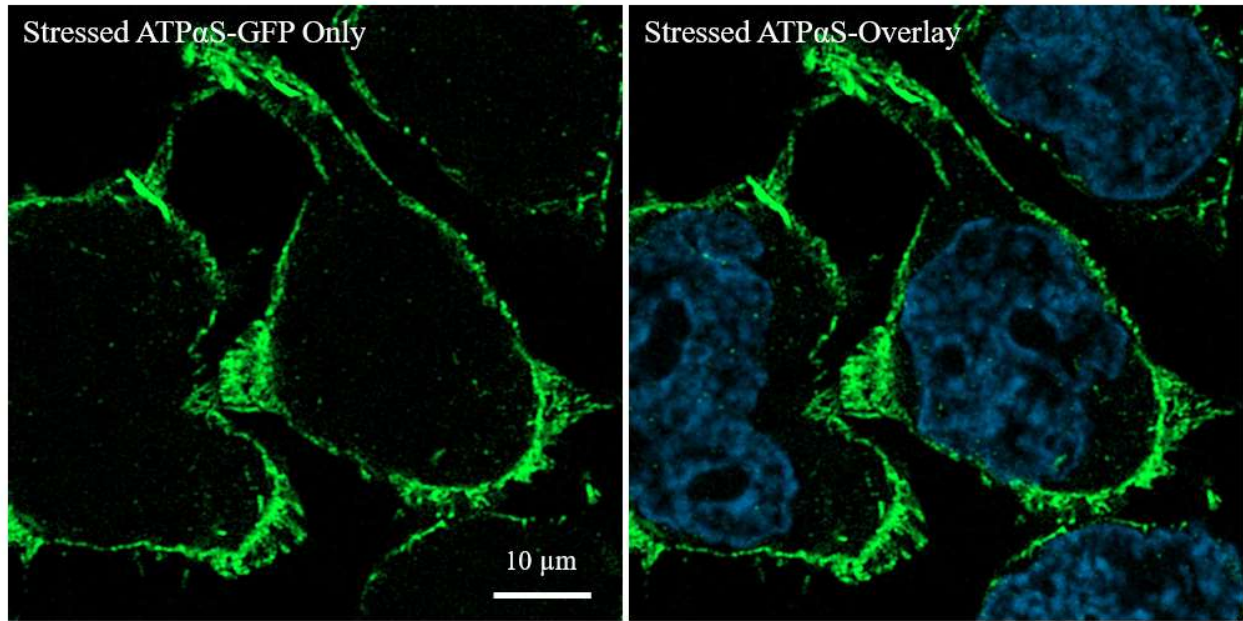Zeiss 700 Confocal microscope images; HeLa cells; ATPγS-Non-stressed (top left & right) and Stressed (4.8 μL; 0.625 M sodium azide: 0.375 M DDG), (bottom left & right) with GFP-only vector (Green) and DAPI (Blue)/GFP (Green) overlay.
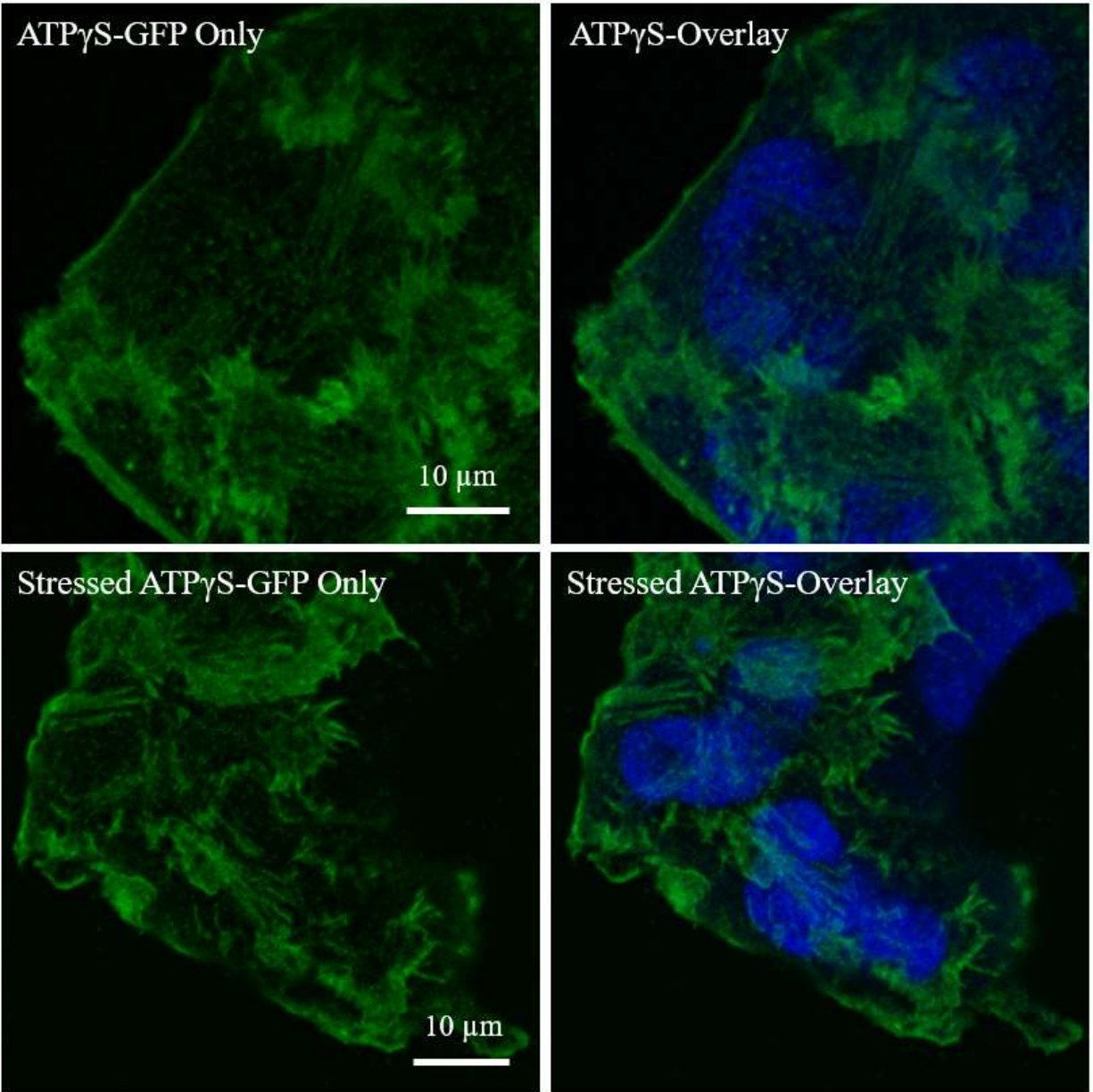
The optogenetic experiments concluded with evidence that suggested that the ATP-αS analogue was the better of the two to in terms of actin rod inhibition based on data seen in **Figures 14 and 15**. Variables in the control data correspond to the variation in the healthy cells per sample with anywhere from 60-90% of the cells exhibiting some kind of clusters after a few seconds of exposure.[9] Slowed cluster formation can be described as any noticeable delay in the onset of clustering as compared to the control (~30sec-1 minute).
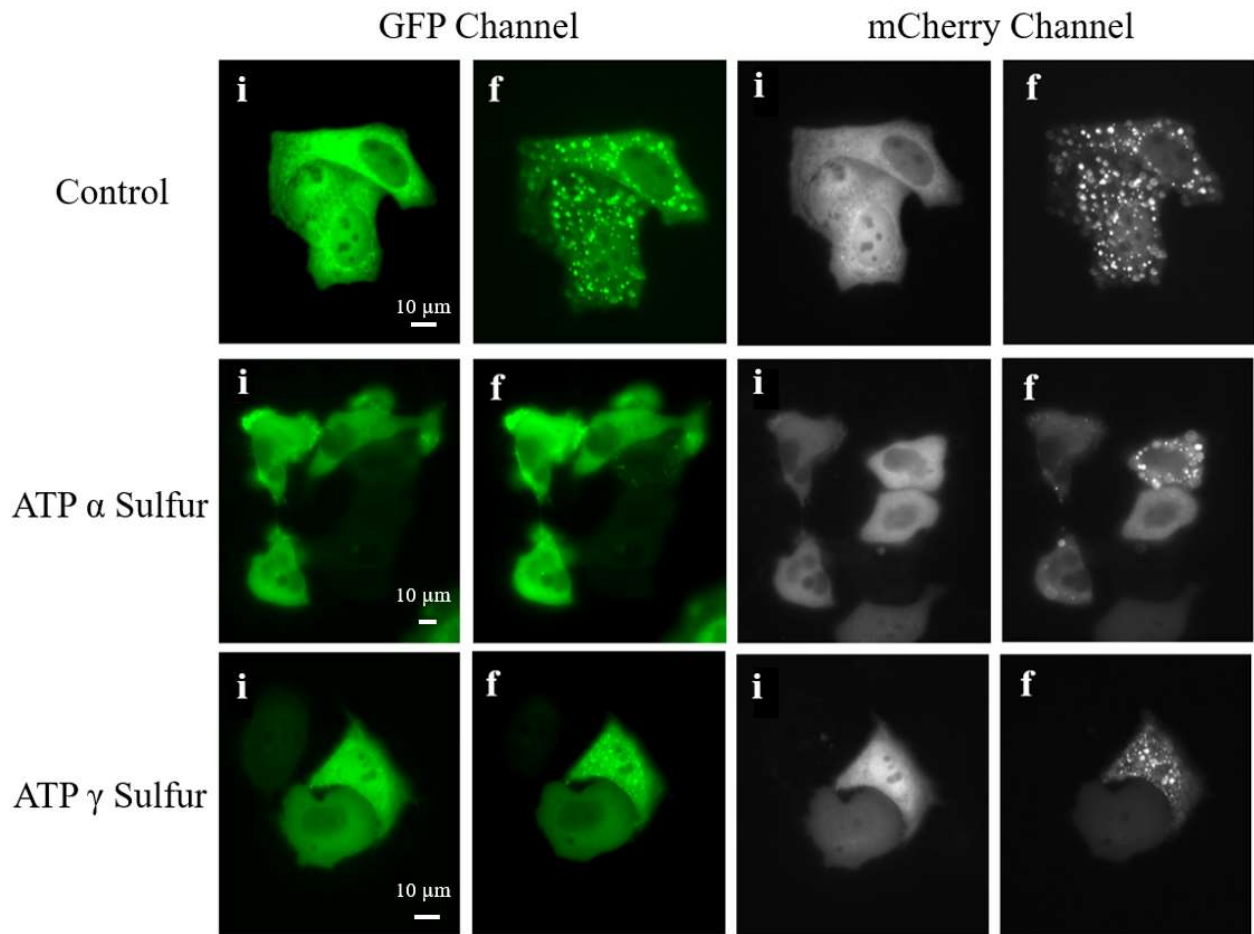
Figure 14: Optogenetic ATP Sulfur Analogue expt
Leica widefield microscope images; Optogenetic experimentation with nonhydrolyzable ATP analogues (1 mM Concentration) under energetic stress conditions (4.8 µL; 0.625 M sodium azide: 0.375 M DDG) on both the GFP (Green) and mCherry (Grey) channels. ATP analogues were double transfected with Actin-CIB-GFP and Cry2-mCherry-S3E Cofilin. (i) is before light activation, (f) is after light activation (30 second intervals of blue light for a 10-minute duration). (1) Oxidant control, (2) ATP α Sulfur, and (3) ATP γ Sulfur.
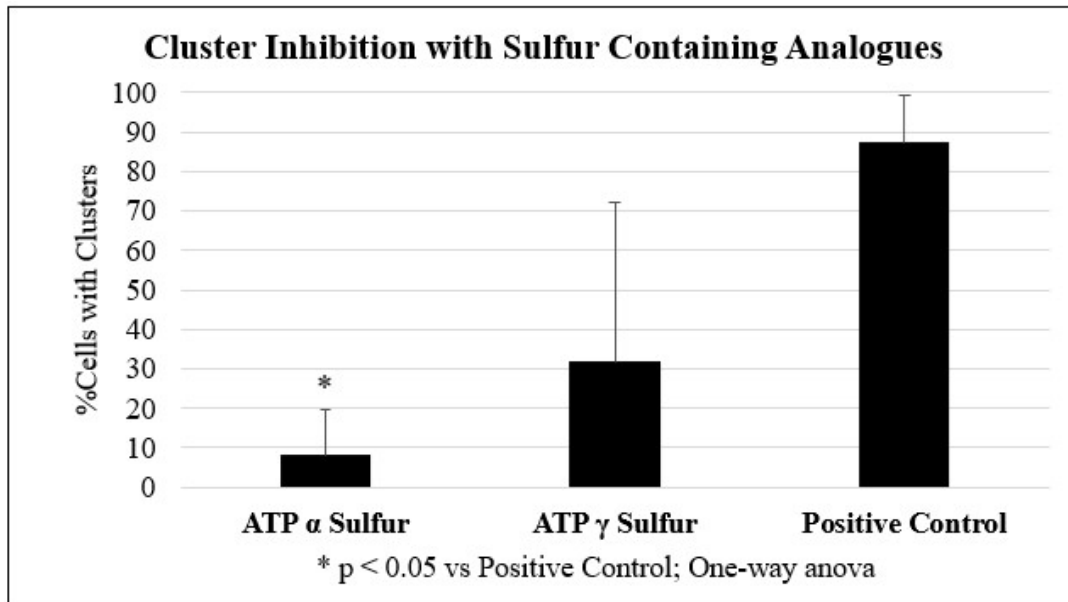
Figure 15: Cluster Inhibition with Sulfur Containing Analogues
Bar graph comparing the optogenetic cluster inhibition capabilities of the sulfur containing nonhydrolyzable ATP analogues where n=20 cells per sample at 4 samples per construct. Control data from source[25] ATP α Sulfur is statistically significant ($p < 0.05$) via a one-way ANOVA compared to the control.

4.2: Concentration Titration and P2X/ P2Y Receptor Hypothesis

Experimental design for this section was the same when preparing the cells for imaging. Concentration of ATP analogues aliquots were prepared from a 10 mM stock for the concentrations higher than 1 mM and a 1 mM stock for the concentrations at and below 1mM. Based on our experimental results seen in **Figure 16**, an oscillation pattern presents itself when moving from the 0 µM control to 50 µM concentration of the ATP analogue where after the percent of cells exhibiting clusters appears to be at a minimum, it has a drastic increase in cells with clusters. However, after 250 µM, the percent of cells with clusters with cells treated with 500 µM concentration of the ATP analogue again drops to a minimum whereas the pattern continues. Once perplexed by this outcome, we came across an ATP gated ion channel that could be the reason behind the odd trend.
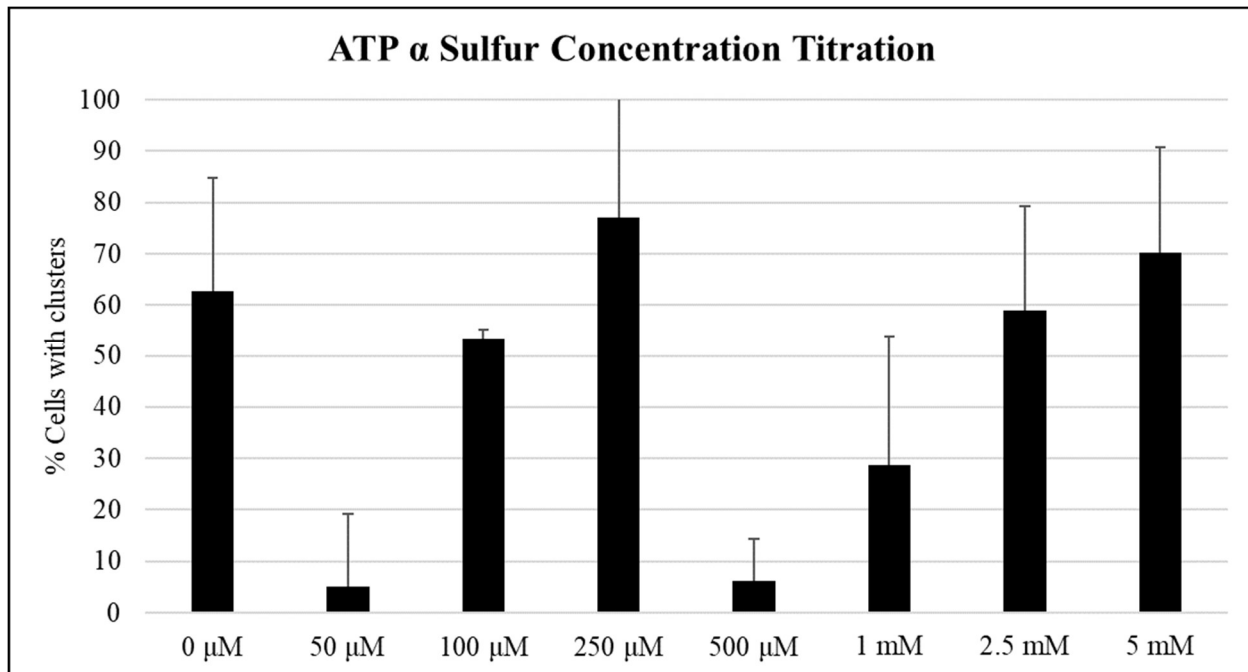
Figure 16: ATP α Sulfur Concentration Titration
Bar graph of ATP α Sulfur analogue concentration titration data where n=50 cells per condition. HeLa cells were transfected with both the Actin-CIB-GFP and CofilinS3E-Cry2-mCherry using Lipofectamine 3000 at 1000 ng of DNA of each fusion for a total of 2000 ng of DNA. Concentration of ATP α Sulfur analogue aliquots were prepared from a 10 mM stock for the concentrations higher than 1 mM and a 1 mM stock for the concentrations at and below 1mM.

As explained before, the P2X and P2Y receptors play a key role in the regulation of the hydrolysis of ATP. Based on our results, it appears that the nonhydrolyzable ATP analogues may be blocking these receptors at specific concentration intervals, specifically at 50 μM and 500 μM seen in **Figure 17**. Results from Bhattacharya et. Al. show selective receptor activations induced Ca^{2+} signals that differed in sites of initiation, kinetics, wave directions and magnitudes of Ca^{2+}-induced Ca^{2+} release.[29] This selective activation were consistent with their experiments for distinct subcellular expression for $P2X_4R$ and $P2X_7R$. These results can be used to explain the phenomenon we experienced in our data that indicated interference with individual P2X purinoceptor subtypes which displayed distinct Ca^{2+} wave initiation. More experiments may be conducted to determine

at exactly what concentrations the P2X receptor is interrupted by conducting concentration titrations with Ca^{2+} indicators.
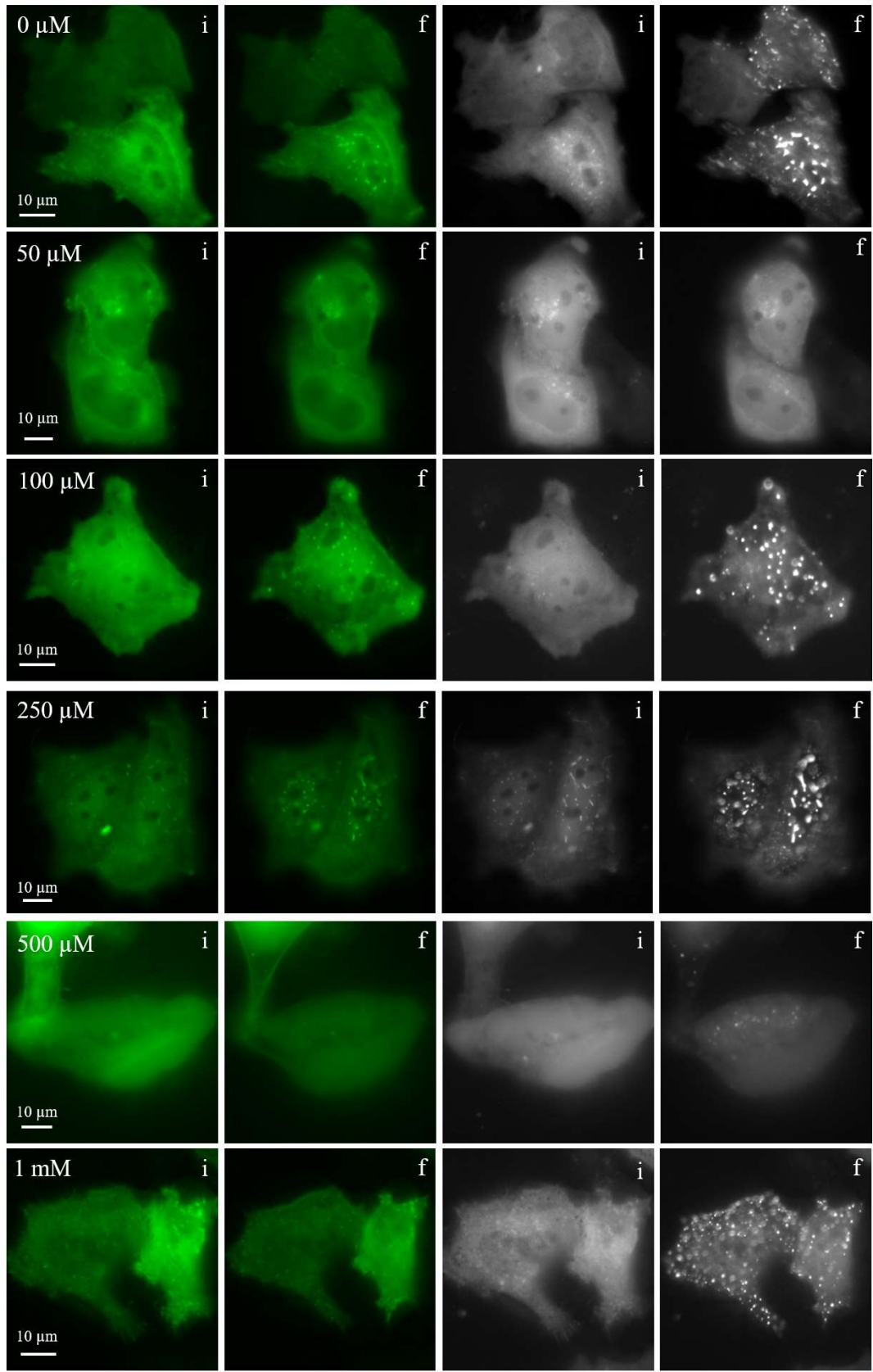
Figure 17: Optogenetic Cluster formation for ATP α Sulfur Concentration Titration
Leica widefield microscope images; Optogenetic Concentration Titration with nonhydrolyzable ATP-αS analogue (0, 50, 100, 250, 500 μM, and 1 mM Concentrations) under energetic stress conditions (4.8 μL; 0.625 M sodium azide: 0.375 M DDG) on both the GFP (Green) and mCherry (Grey) channels. Cell samples were double transfected with Actin-CIB-GFP and Cry2-mCherry-S3E Cofilin. (i) is before light activation, (f) is after light activation (30 second intervals of blue light for a 10-minute duration).

Chapter 5:   Cofilin Peptide Characterization and Mutagenesis

My main objective will be to use optogenetic techniques to stimulate protein clusters in stress conditions to monitor the presence of actin-cofilin rods. The goal of this aim is to localize a small cofilin-like peptide on actin through its cofilin binding sites for inhibition of actin-cofilin rods, or as actin biomarker peptides that do not have adverse side effects on actin dynamics. Based on structural information given in previous studies[26], cofilin has three binding domains as shown in **Figure 18**; F-site 1, 2 and G-site. The complete amino acid sequence is given in the description.
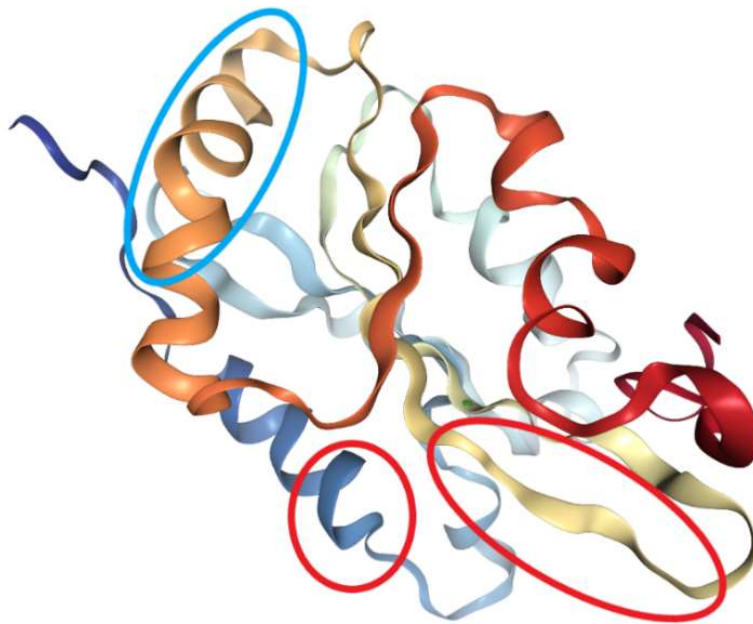
Figure 18: 3D structure of Cofilin-1
The blue being the N-terminus and red being the C-terminus. The blue circle indicates the G-binding site and the two red circles indicate both the α-helix and β-sheet F-binding sites, F-1 and F-2 binding sites respectively (Figure from structural data from Protein Data Bank (PDB)).[34]

Amino acid sequence: **F-binding sites   G-Binding site**
MASGVAVSDGVIKVFN**DMKVRKS**STPEEVKKRKKAVLFCLSEDKKNIILEEGKEILVGD
VGQTVDDPYATFVKMLPDKDCRYALYDATYETKES**KKEDLVFIFW**APESAP**LKSKMI**
YASSKDAIKKKLTGIKHELQANCYEEVKDRCTLAEKLGGSAVISLEGKPL

*Using this information, primers were constructed for the specific sections listed in **Table 1**.*

Table 1: Cofilin Fragment Formation
Cofilin-1 sections selected for experimental investigations. All primers were ordered with a GFP tag off the C-terminus of the fragment. All fragments starting from the N-terminus were tested in the optogenetic experiments using the MAA mutation and the wild type MAS configuration.

Name: Length-First 3-Last 3	Amino acid sequence α-helix β-sheet **Bold-** Binding site
Short: 19-MAA-DMK	MAAGVAVSDGVIKVFN**DMK**
Long: 31-MAA-VKK	MAAGVAVSDGVIKVFN**DMK**VRKSSTPEEVKK
F-α-helix (59N): 59-MAA-VGD	MAAGVAVSDGVIKVFN**DMK**VRKSSTPEEVKKRKKAVLFCLSEDKKNIILEEGKEILVGD
F-β-sheet (48AA): 48-VGQ-APE	VGQTVDDPYATFVKMLPDKDCRYALYDATYETKES**KKEDLVFIFW**APE
G-α-helix (59C): 59-NAP-KPL	NAP**LKSKMIYASSKDAIKKK**LTGIKHELQANCYEEVKDRCTLAEKLGGSAVISLEGKPL
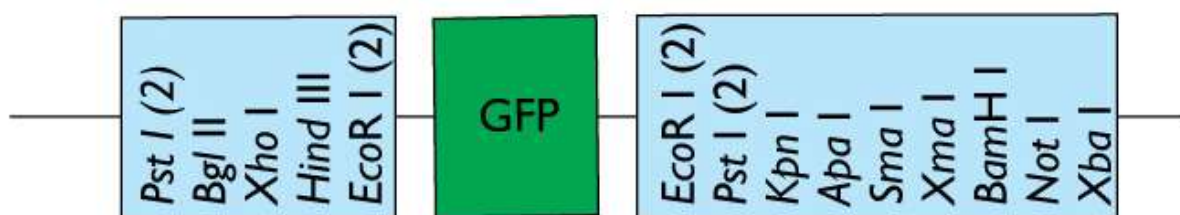
Figure 19: phCMV-NGFP Vector
All Peptide primers were constructed to be between the Xho1 and Hind III sites to include the GFP tag on the C-terminus of the peptide using the phCMV-NGFP vector.[35]

Table 2: Cofilin Fragment Primers
Primers based between Xho I and Hind III sites of the phCMV-NGFP vector.

Peptide Primer	Forward Reverse
Cof-Short	GTTACC CTCGAG ATGGC CTCGGTGTG GC AATTCG AAGCTT CG GCTGCCGCCGCTGCCGCC CTT CAT GTC ATT GAA CAC C
Cof-Long	GTTACC CTCGAG ATGGC CTCGGTGTG GC AATTCG AAGCTT CG GCTGCCGCCGCTGCCGCC TTTCTTCACTTCTTCTGG
59N	GTTACC CTCGAG ATGGC CTCGGTGTG GC AATTCG AAGCTT CG GCTGCCGCCGCTGCCGCC ATC TCC TAC CAG GAT CTC
48AA	GTTACC CTCGAG ATG GTG GGG CAG ACT GTG GAC AATTCG AAGCTT CG GCTGCCGCCGCTGCCGCC CTC GGG GGC CCA GAA GAT
59C	GTTACC CTCGAG ATG AAT GCA CCC CTC AAG AGC AATTCG AAGCTT CG GCTGCCGCCGCTGCCGCC CAA AGG CTT GCC CTC CAG

5.1: Experimental Design

A PCR (New England Biosciences, Q5 Polymerase) was conducted with forward and reverse primers (**Table 2**) for each of the proposed sections and an 1% agarose gel was run to

separate the DNA bands. The DNA was then extracted from the gel and a DNA ligation reaction was conducted using T4 DNA ligase (10 µL total; T4 DNA ligase 1 µL, T4 Ligase buffer 1 µL, Vector 1 µL, Insert (PCR product) 4 µL, deionized distilled water 3 µL) and let sit at 4°C overnight.

A bacterial transfection was conducted with competent E. coli cells. Aliquots (200 µL) of competent E. coli cells were placed in 1.5 mL tubes, the ligation reaction product (4 µL) was added and allowed to sit on ice for 30 minutes. The mixture was heat shocked at 42°C for 30 seconds and recovered on ice for 2 minutes. Super Optimal Broth (SOC) media (500 µL) was added to the cells and allowed to shake for 1 hour at 37°C. The cells were then plated (300 µL) on a Kanamycin resistant plate and incubated at 37°C overnight. A MINI prep was conducted on the cells to isolate the DNA and checked for accuracy using a Diagnostic PCR. These sections were sent for sequencing.

The cofilin were then tested using a test transfection using the MINI prep product (~2000 ng of DNA). For a 6-well plate size transfection reagent procedure, 5 µL of P3000 was added to the DNA. In a separate container, 125 µL of Opti-MEM and 3.75 µL Lipofectamine 3000 reagent per sample were mixed to make a stock. The reagent stock (~127 µL per sample) was added dropwise to an aliquot of HeLa cells with a GFP control sample and allowed to incubate at 37°C overnight. The next day the cells were imaged using a confocal microscope.

For optogenetic experiments, the cofilin fragments were kept with the GFP tag. However, to open the GFP channel for other imaging applications on the cofilin fragments, the GFP tag on the Actin-CIB-GFP construct had to be removed. Using the same concept and the 6-well plate size Lipofectamine 3000 procedure, the fragment (1000 ng, Fragment-GFP), Actin-CIB-STOP (1000 ng) and CofilinS3E-Cry2-mCherry (1000 ng) were triple transfected into a HeLa cell

34

concentration of (~200,000 cells/mL) and incubated at 37°C overnight. Before imaging on the Leica Fluorescence microscope, the cells were treated with the stress inducing solution for 5 minutes.

For fixed cell experiments, the cells were single transfected with 2000 ng of DNA from the cofilin fragments. The next day, the media was aspirated from the HeLa cells and washed with 1 mL of DPBS. The cells to be treated were removed from the incubator and 1 mL of the stress inducing solution (0.01 M sodium azide: 0.006M DDG) was added to the cells and incubated at 37°C for 1 hour. The cells were removed from the incubator and washed with 1 mL of DPBS and 1 mL of pre-warmed fixative (37°C; 4% PFA (Electron Microscopy Sciences and DPBS)) and allowed to sit at room temperature for 45 minutes. The fixative was removed, and the cells were washed with DPBS, covered in 1.5 mL of DPBS, wrapped in parafilm and placed in the refrigerator until ready to perform the immunostaining.

For the immunostaining process, the cells were permeabilized for 3 minutes with pre-chilled methanol (-20°C) then blocked for 30 minutes with CST Ab dilution buffer (30 μL Triton X-100, 0.1 g of BSA, and 10 mL of DPBS) and incubated overnight at 4°C with primary mouse actin antibody and 1:500 in Ab dilution buffer. The following day, the primary antibody solution was removed via pipette and washed 3 times with 1 mL of DPBS. The cells were then incubated with anti-mouse Texas Red for 1 hour at room temperature followed by a wash with DPBS (3 times) and stored in 1.5 mL of DPBS and a DAPI stain was applied before imaging. The images were collected on a Zeiss Confocal microscope.

5.2: Actin Localization Under Stressed Conditions

Though very slight, the cofilin "Long" fragment gave promising results as there was evidence of cofilin concentrations around the membrane of the cells as seen in the imaging data in Figure 20 below.
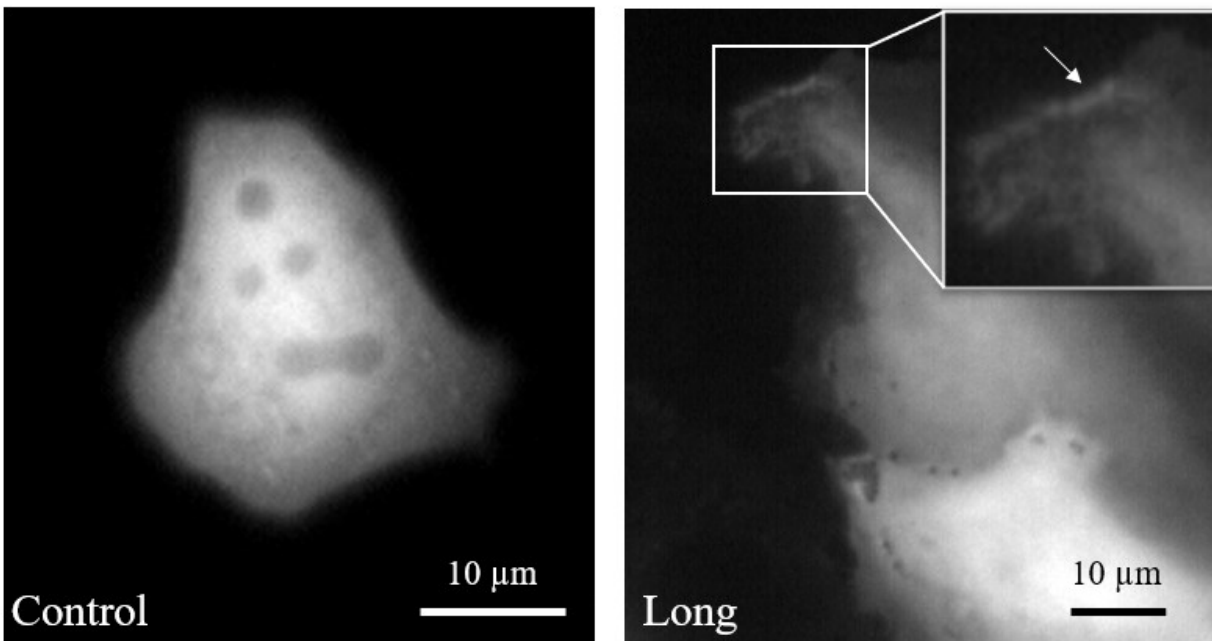
Figure 20: Change in Peptide Localization
Leica widefield microscope; Transfected HeLa cells on the GFP channel (Grey) with the cofilin Long fragment found in **Table 1** (including GFP) and a control (GFP vector only). Notice the localization along the edges as compared to the control.

When observing the short fragment transfected cells, the change in the cell's GFP concentration when compared to the GFP control did not exhibit any change as compared to the long fragment transfect cells. This led us to breaking the cofilin-1 protein down further into other sections based on the binding sites of cofilin to actin to investigate for protein binding to these sites during the stress conditions when actin-cofilin rods should form. The fragments used in the experiments were based on cofilin's F and G binding sites to actin (Shown in **Figure 18** and **Table 1**). Using fixed cell experiments using actin immunostaining, we were able to observe the overlay with the

fragments and actin with and without the stress conditions. From the native actin localization experiments including the transfection of the fragments shown in **Figures 21-26**, it is speculated that before stress conditions, the long and 59C fragments can bind to actin at the F and G-site and can stay bound even after the stress solution is applied. The short, 48AA and 59C fragments show no signs of actin localization before or after the stress conditions. These observations are represented in **Table 3**.
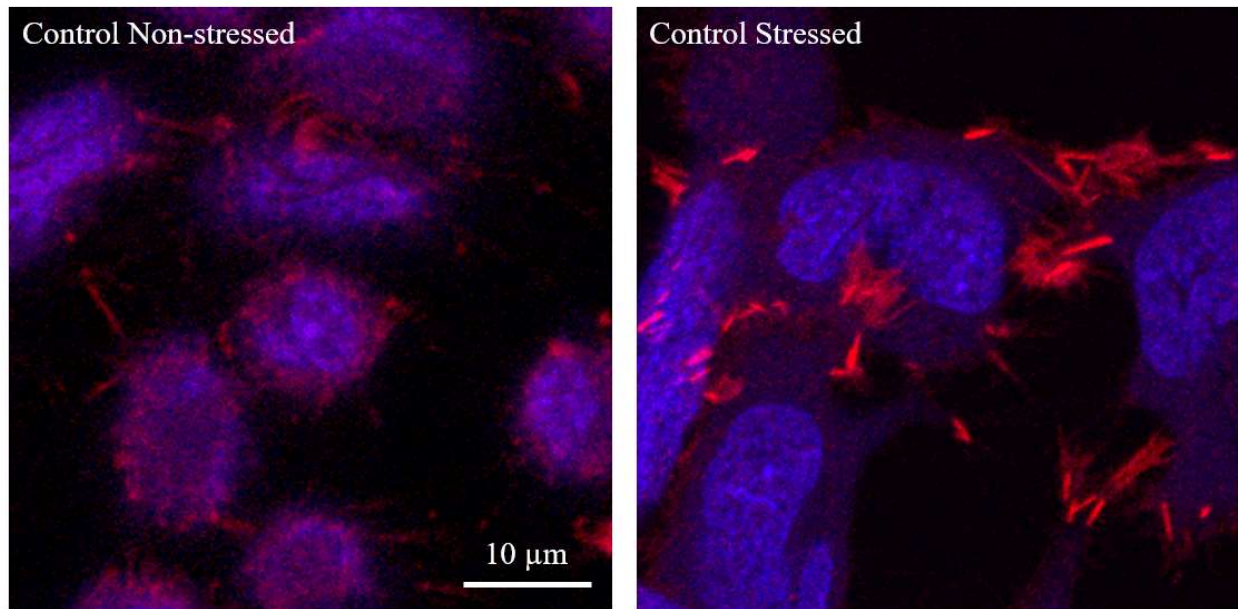
Figure 21: Cofilin Peptide Fragment expt; Control
Zeiss 700 Confocal microscope images; Control Non-stress and stressed conditions (1 mL; 0.01 M sodium azide: 0.006 M DDG, 1 hr). Immunostained with both DAPI (Blue) and actin primary antibody-Texas Red (Red).
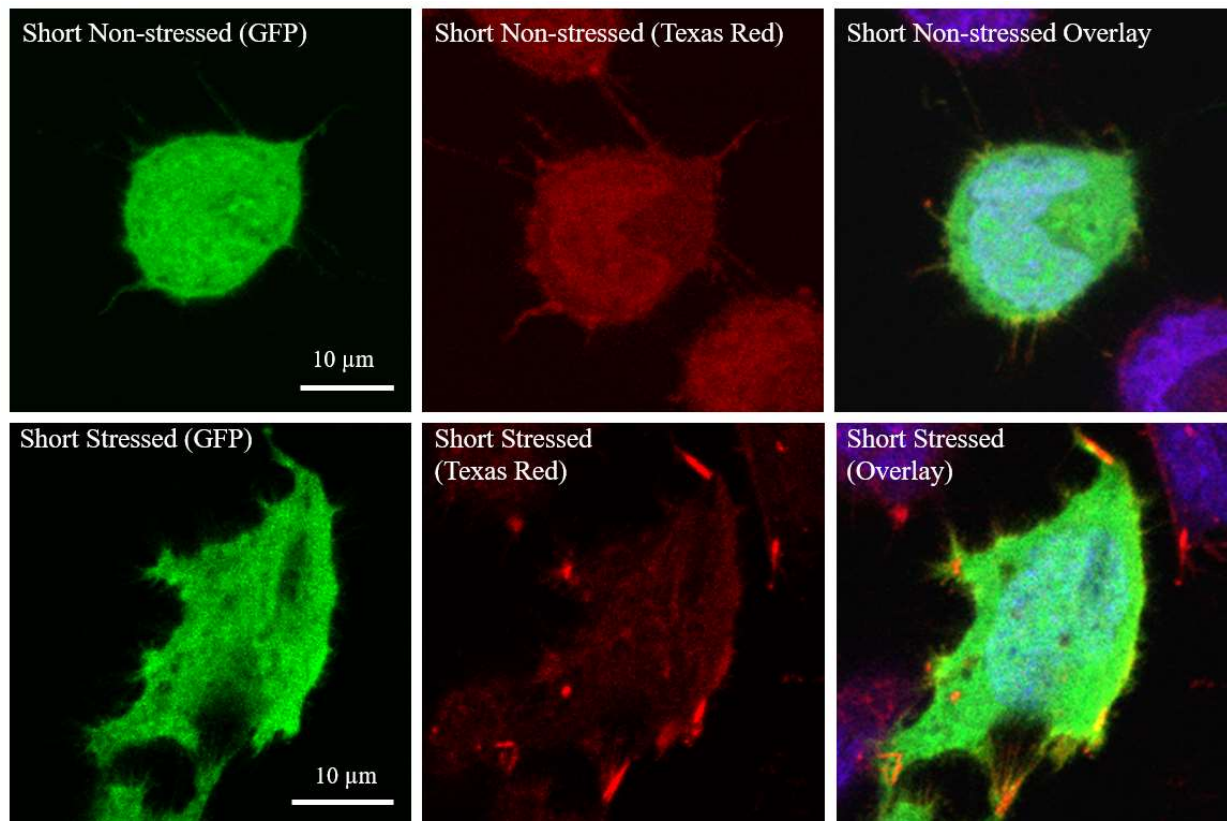
Figure 22: Cofilin Peptide Fragment expt; Short
Zeiss 700 Confocal microscope images; Short fragment (from left to right) Non-stressed GFP channel (Green), Texas Red channel (Red), and Overlay (GFP, Texas Red, DAPI (Blue)); stressed conditions (1 mL; 0.01 M sodium azide: 0.006 M DDG, 1 hr) GFP channel, Texas Red channel, and Overlay.
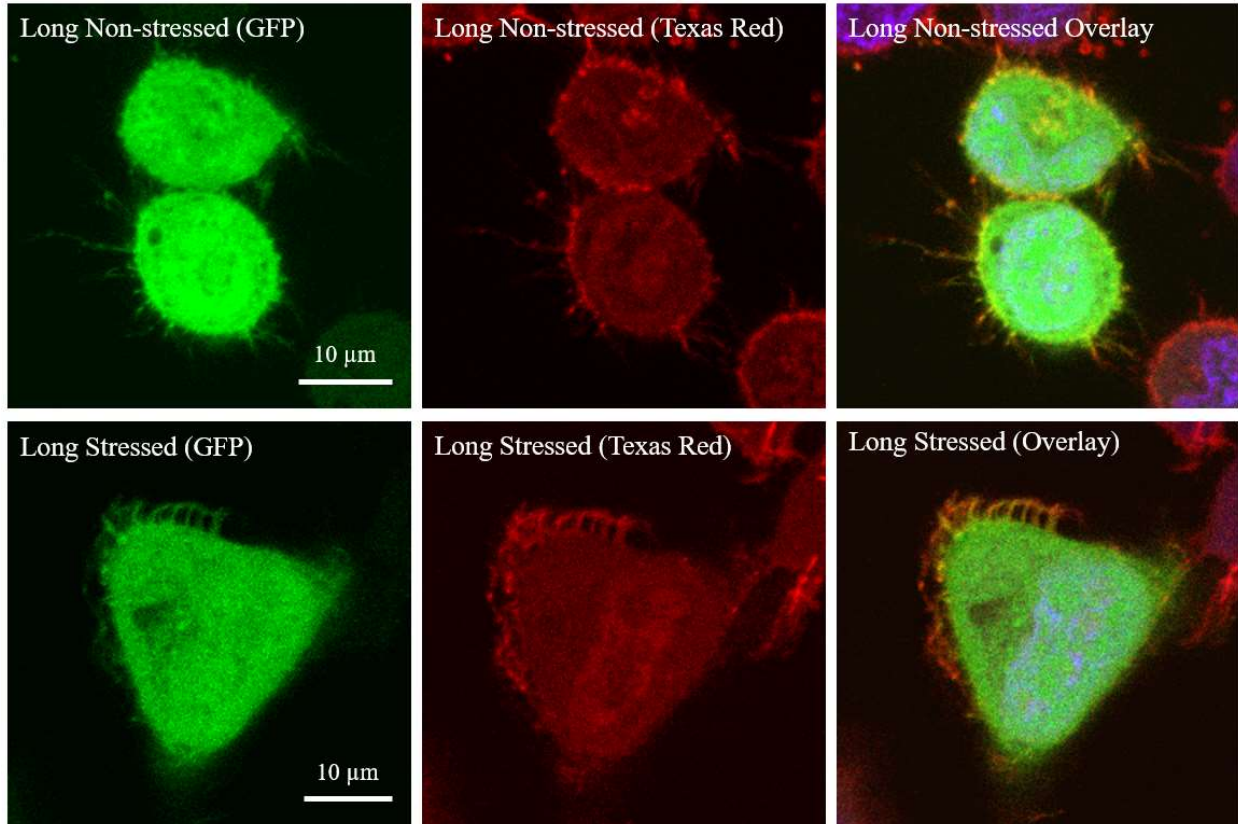
Figure 23: Cofilin Peptide Fragment expt; Long
Zeiss 700 Confocal microscope images; Long fragment (from left to right) Non-stressed GFP channel (Green), Texas Red channel (Red), and Overlay (GFP, Texas Red, DAPI (Blue)); stressed conditions (1 mL; 0.01 M sodium azide: 0.006 M DDG, 1 hr) GFP channel, Texas Red channel, and Overlay.
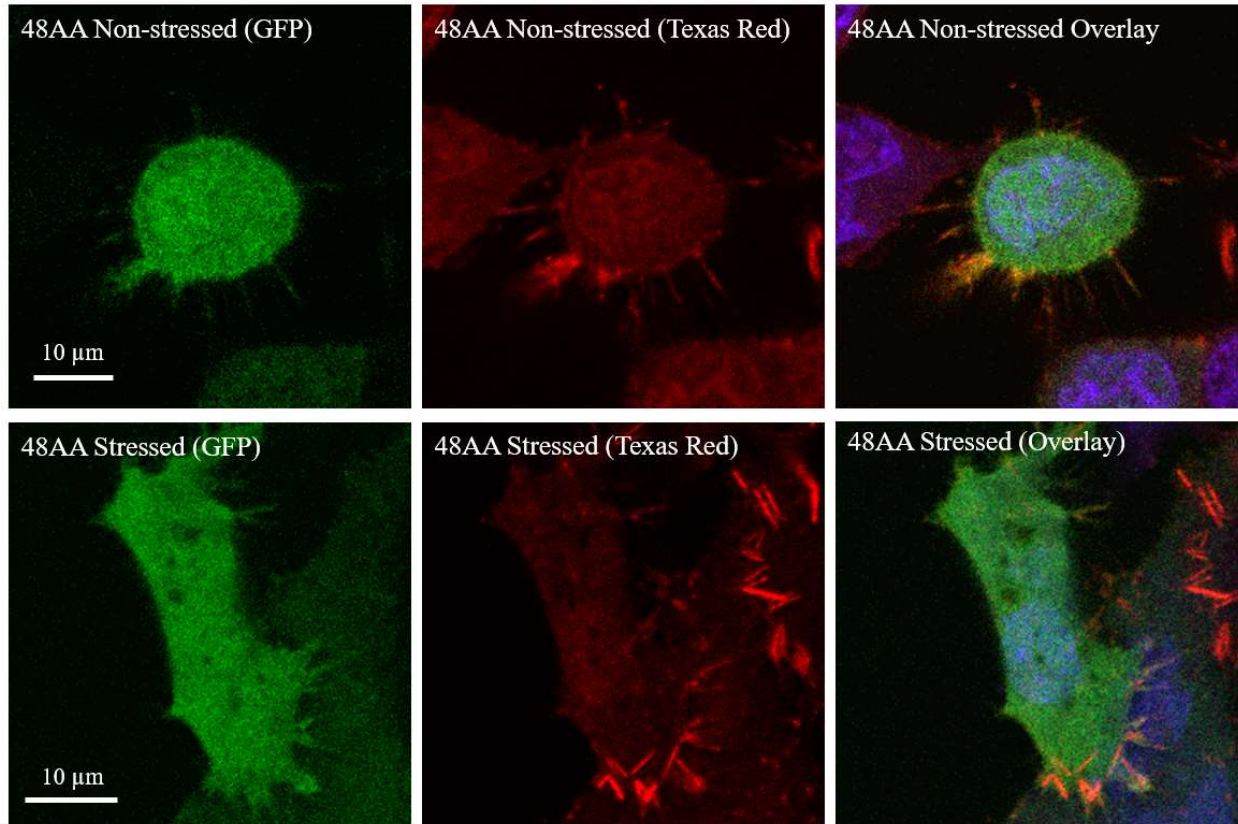
Figure 24: Cofilin Peptide Fragment expt; 48AA
Zeiss 700 Confocal microscope images; 48AA fragment (from left to right) Non-stressed GFP channel (Green), Texas Red channel (Red), and Overlay (GFP, Texas Red, DAPI (Blue)); stressed conditions (1 mL; 0.01 M sodium azide: 0.006 M DDG, 1 hr) GFP channel, Texas Red channel, and Overlay.
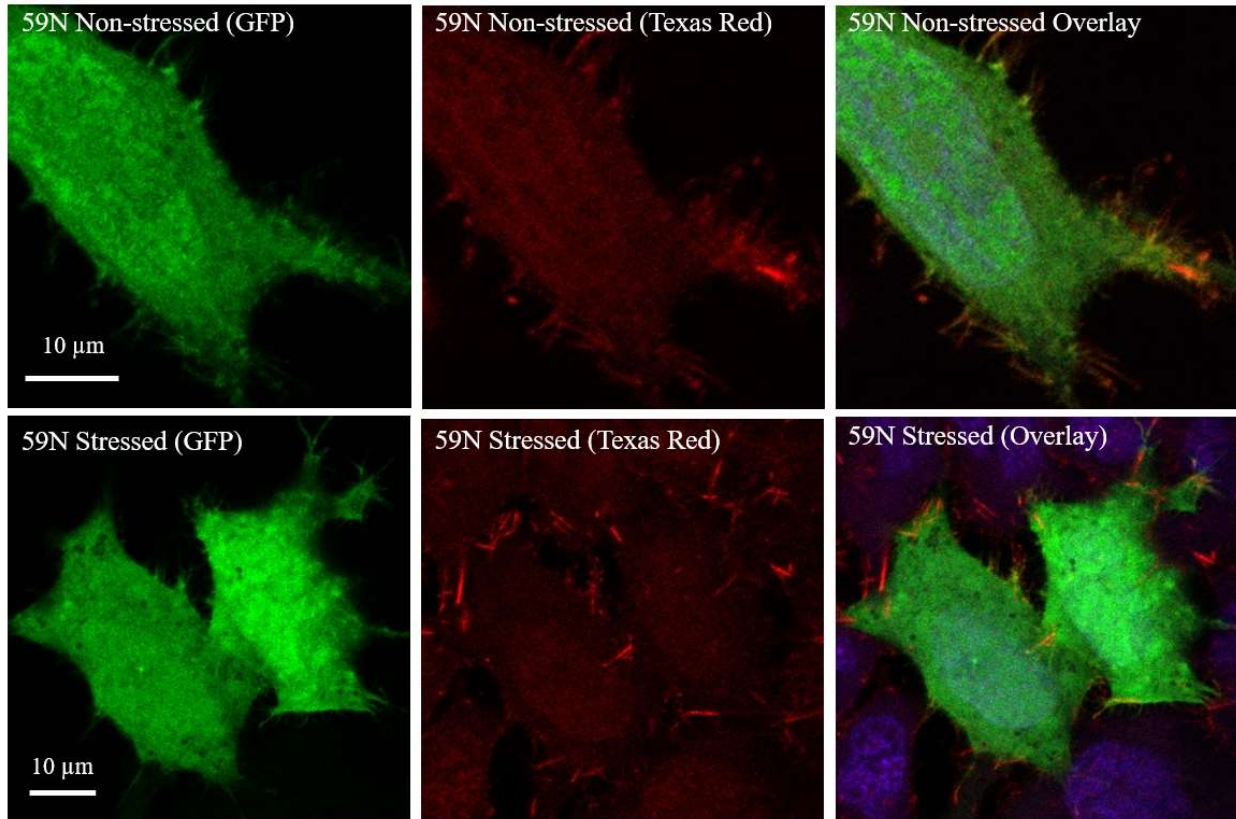
Figure 25: Cofilin Peptide Fragment expt; 59N
Zeiss 700 Confocal microscope images; 59N fragment (from left to right) Non-stressed GFP channel (Green), Texas Red channel (Red), and Overlay (GFP, Texas Red, DAPI (Blue)); stressed conditions (1 mL; 0.01 M sodium azide: 0.006 M DDG, 1 hr) GFP channel, Texas Red channel, and Overlay.
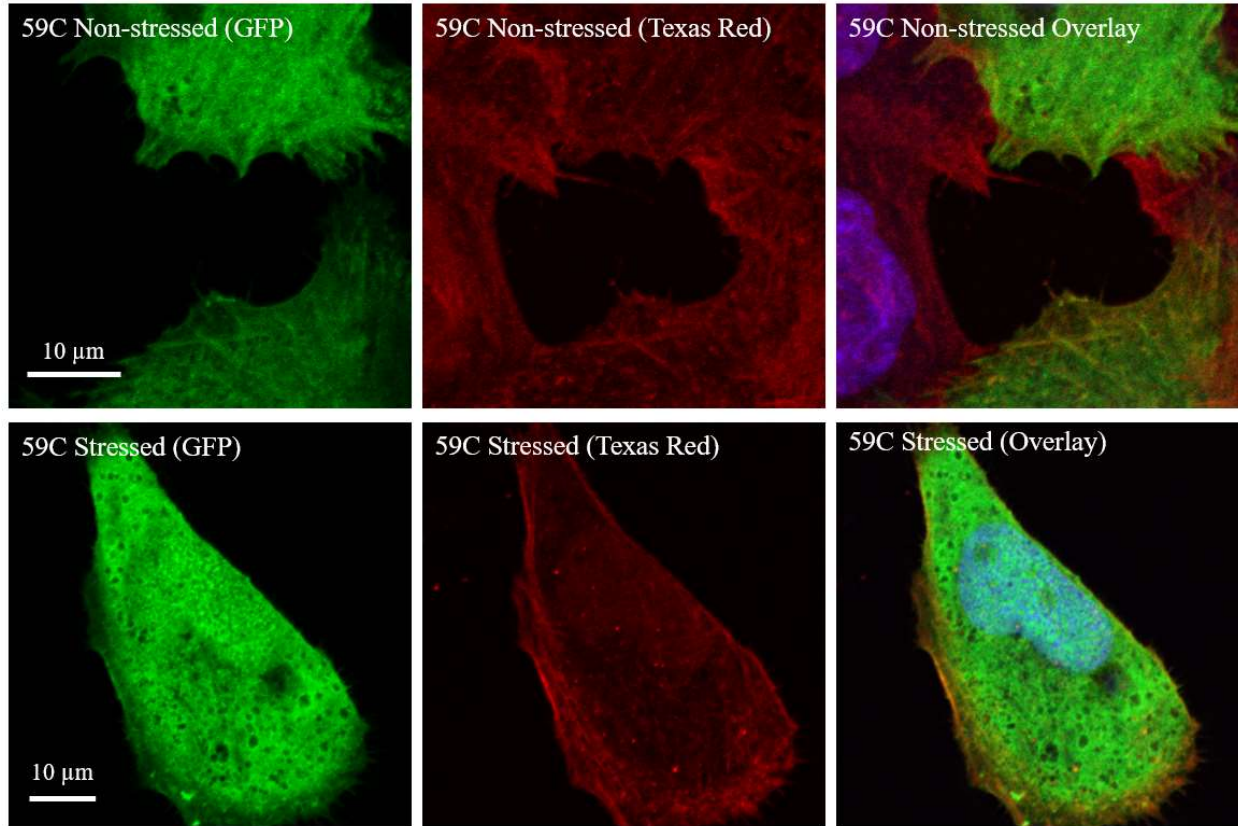
Figure 26: Cofilin Peptide Fragment expt; 59C
Zeiss 700 Confocal microscope images; 59C fragment (from left to right) Non-stressed GFP channel (Green), Texas Red channel (Red), and Overlay (GFP, Texas Red, DAPI (Blue)); stressed conditions (1 mL; 0.01 M sodium azide: 0.006 M DDG, 1 hr) GFP channel, Texas Red channel, and Overlay.

Table 3: Cofilin Fragment Localization Patterns
Observed properties of cofilin fragments before and after the introduction of stressed conditions

Cofilin Fragments	Actin Localization	Actin Localization – Stressed Conditions	No actin localization
Short			X
Long	X	X	
48AA			X
59N			X
59C	X	X	

42

The 59C fragment contains a binding site of cofilin that shares some binding residues in the Go-site of actin (residues 341–342, 345–346, 348–351, 355)[26] to a known F-actin binding protein called "LifeAct" that is also in a similar α-helix structure.[36]
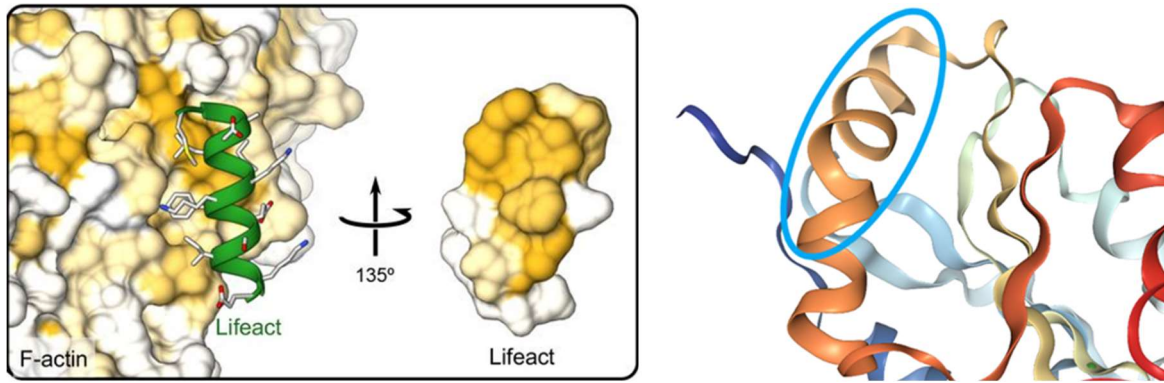
Figure 27: LifeAct to Cofilin Comparison
LifeAct bound to F-actin (Left) as compare to the G-site α helix found in cofilin and the 59C fragment (Right) made for these experiments (Figure from Belyy et. Al. 2020).[37]

LifeAct has had some side effects that have been exhibited during its use as an F-actin biomarker that could potentially cause unwanted cellular activities to occur such as impacting actin stress dynamics and cytoskeletal network failures caused by an unwanted redetection in the native binding affinity of cofilin to actin.[38,39] Further research into and mutations of this fragment may bring to light a peptide sequence that has the same binding affinity to actin without the unwanted artifacts of LifeAct.

Chapter 6:   HEK 293T Cell Line used for More Abundant Triple-Transfected Cells

During the previously mentioned experiment involving a HeLa cell model, the experimental data was, at times, difficult to discern. This is mostly due to consistent lack of transfection efficiency through all experiments with co- and triple transfections in the HeLa cell model. To combat this and to have another cell line to compare my findings to, I had decided to include the HEK-293T cell line in my investigation of actin-cofilin rod inhibition. Many researchers today use the HEK-293T cell line because of its high transfection rate.[40,41] I used the same procedures that were used in the nonhydrolyzable ATP and cofilin fragment HeLa cell line experiments to observe whether my results were reproducible or if the new cell line will give me something new entirely with a much better transfection efficiency.

6.1: Experimental design

A small dish of HEK-293T cells (~200,000 cells/mL) was prepared. Before imaging, the cells will be washed and saturated with DPBS. After initial imaging, 4.8 µL of the stress inducing solution will be added to the cells and incubated at 37°C for 15 minutes and imaged again to monitor changes. The cells will be transfected with the fragments 1 day prior to stress treatment using the Lipofectamine 3000 protocol leaving one control and one stressed control. Again, prior to imaging, the cells will be washed and saturated with DPBS. After the initial imaging, the cells will be treated with the stress inducing solution, incubated for 5 min, and then imaged to monitor localization changes. For fixed cell experiments, 1 mL of the stress inducing solution (0.01 M sodium azide: 0.006M DDG) will be added to the cells and incubated at 37°C for 1 hour. After incubation, the cells will proceed to the immunostaining process as described before.

For optogenetic experiments, the stress procedure is identical to the previous stress treatments. However, during the transfection step the process will include an extra step for the cofilin fragments. The cells for the nonhydrolyzable ATP analogues will be co-transfected with the Actin-CIB-GFP (1000 ng) and CofilinS3E-Cry2-mCherry (1000 ng) and will be imaged before and after stress solution treatment to monitor cluster formation. The cells for the cofilin fragment experiments will need to be triple transfected with the fragment (1000 ng, Fragment-GFP), Actin-CIB-STOP (1000 ng) and CofilinS3E-Cry2-mCherry (1000 ng). This will be the key steps in observing differences between the HeLa cell model and the HEK-293T cell model.

6.2: Results

We have yet to determine whether the characteristics observed in the cell images are due to the influence of the introduced peptides or ATP analogues or if it is due to the HeLa cells being a cancerous cell model. This may need to be investigated further with using the HEK 293T cell line or trying to introduce these peptides and small molecules into neuronal cells directly to investigate any potential changes in the results. The majority of the optogenetic experiments encountered a lack of transfection efficiency making correctly double and, more abundantly, triple transfected cells difficult to observe. To combat this, I intend to duplicate the experiments in the HEK-293T cell line as it has a much higher transfection rate[41] which could give us a larger array of data points to compare to my initial findings.

6.3: Optogenetic Analysis with Peptide Mutations

After actin localization and stressed conditions were observed, I wanted to investigate the possibilities of mutating the G-binding site of the 59C fragment. I also wanted to use the CofActor system with 59C fragment, and its mutations as compared to that of the "Long" fragment which

showed potential actin localization before and after the stressed conditions. This gave some interesting data regarding the overall cluster inhibition relative to the GFP intensity. With a lack of data points for intermediate GFP intensity to cluster formation, it was hard to discern a solid contradiction between the "Long" and 59C fragments. However, these two fragments did follow a pattern in contrast to the 59N fragment which, as previously mentioned, had shown no signs of actin localization before or after stress conditions. The results of these experiments can be seen in figures 28-31 where the samples were triple-transfected with an Actin-CIB-STOP, Cry2-mCherry-S3E Cofilin, and either an empty GFP vector (control) or a fragment-GFP fusion. Each experiment was conducted in HEK 293T cells, at the addition of the energetic stress solution, and exposed to blue light at 30-second intervals for a 10-minute duration.

Figure 28: Optogenetic Cofilin Peptide expt; Control
Leica widefield microscope images; Peptide transfection optogenetic experimentation, Control cells under energetic stress conditions. From left to right; mCherry channel (Grey) before and after light exposure and a GFP transfection affirmation (Green).
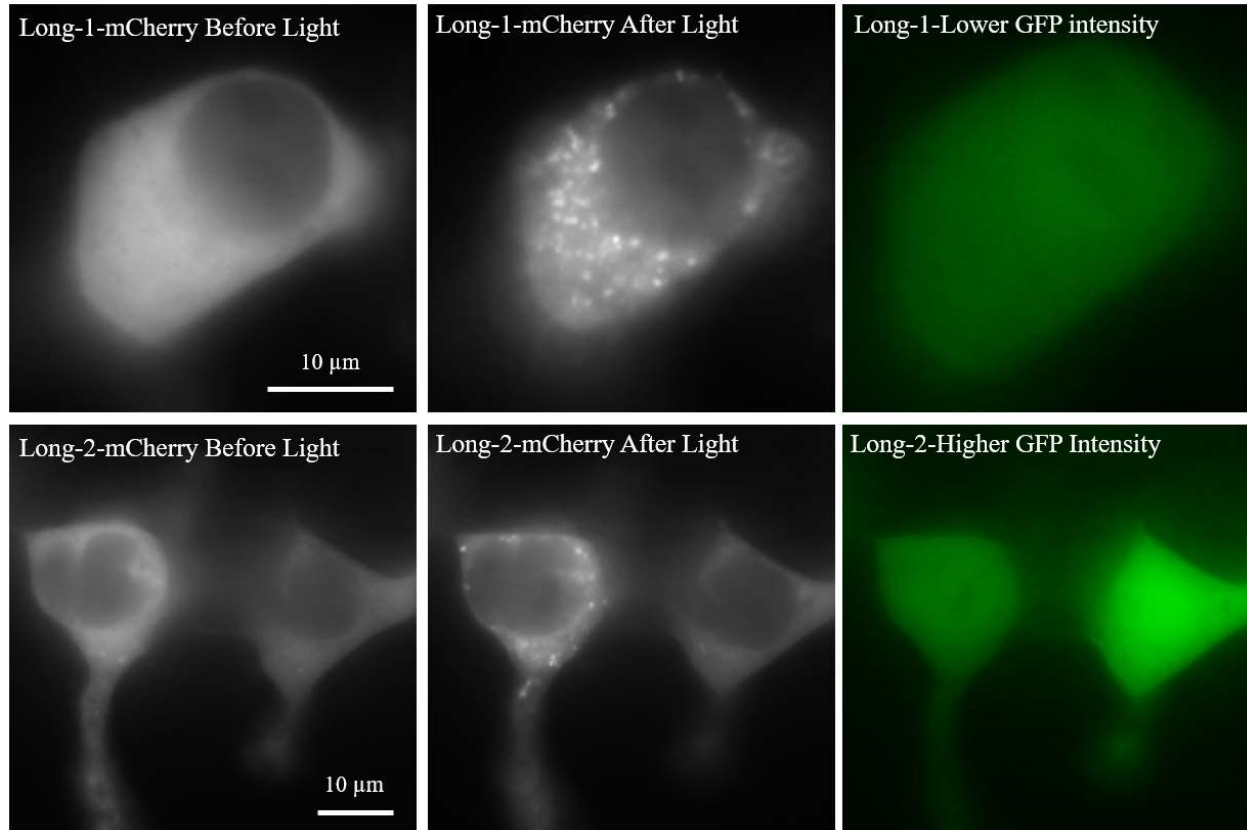
Figure 29: Optogenetic Cofilin Peptide expt; Long
Leica widefield microscope images; Peptide transfection optogenetic experimentation, Long fragment transfected HEK 293T cells under energetic stress conditions. From left to right, top to bottom; mCherry channel (Grey) before and after light exposure and a GFP transfection affirmation (Green) with a lower and higher GFP intensity respectively.

Figure 30: Optogenetic Cofilin Peptide expt; 59N
Leica widefield microscope images; Peptide transfection optogenetic experimentation, 59N fragment transfected HEK 293T cells under energetic stress conditions. From left to right, top to bottom; mCherry channel (Grey) before and after light exposure and a GFP transfection affirmation (Green) with a lower and higher GFP intensity respectively.
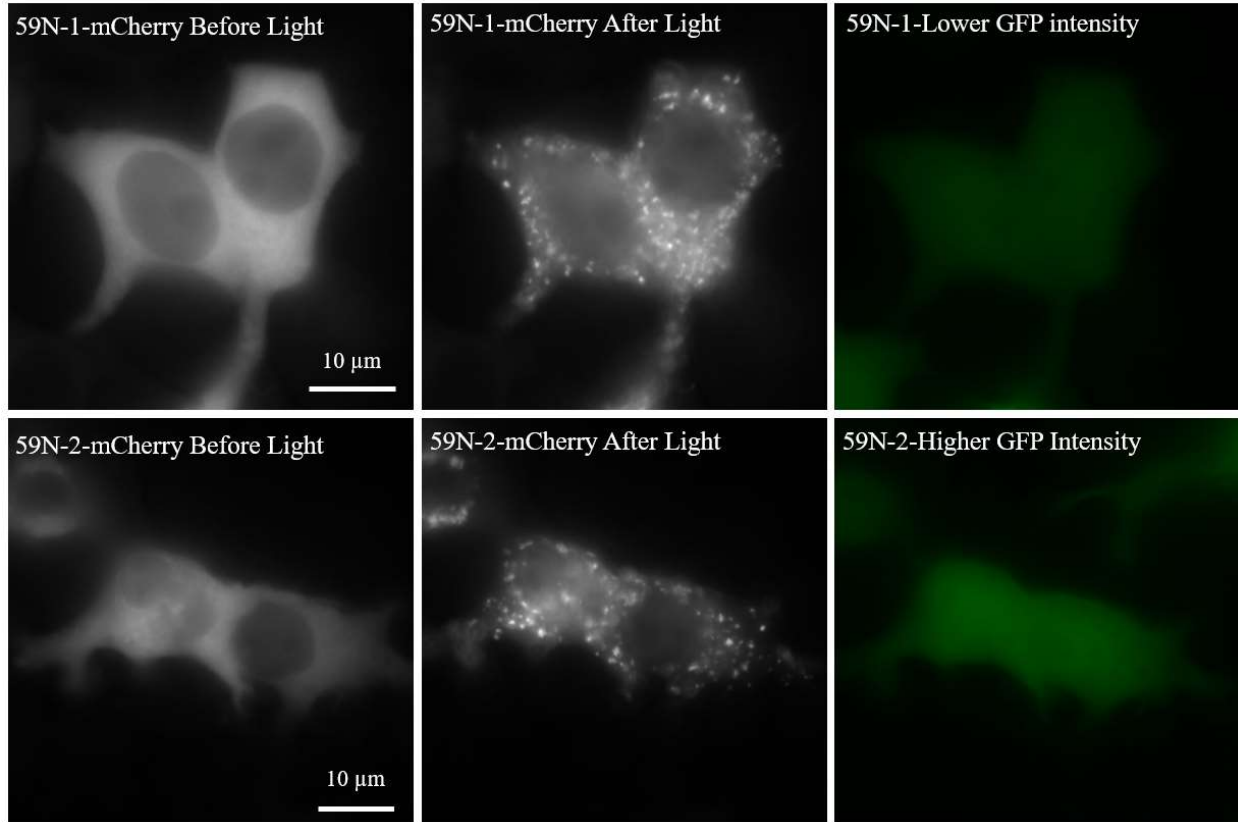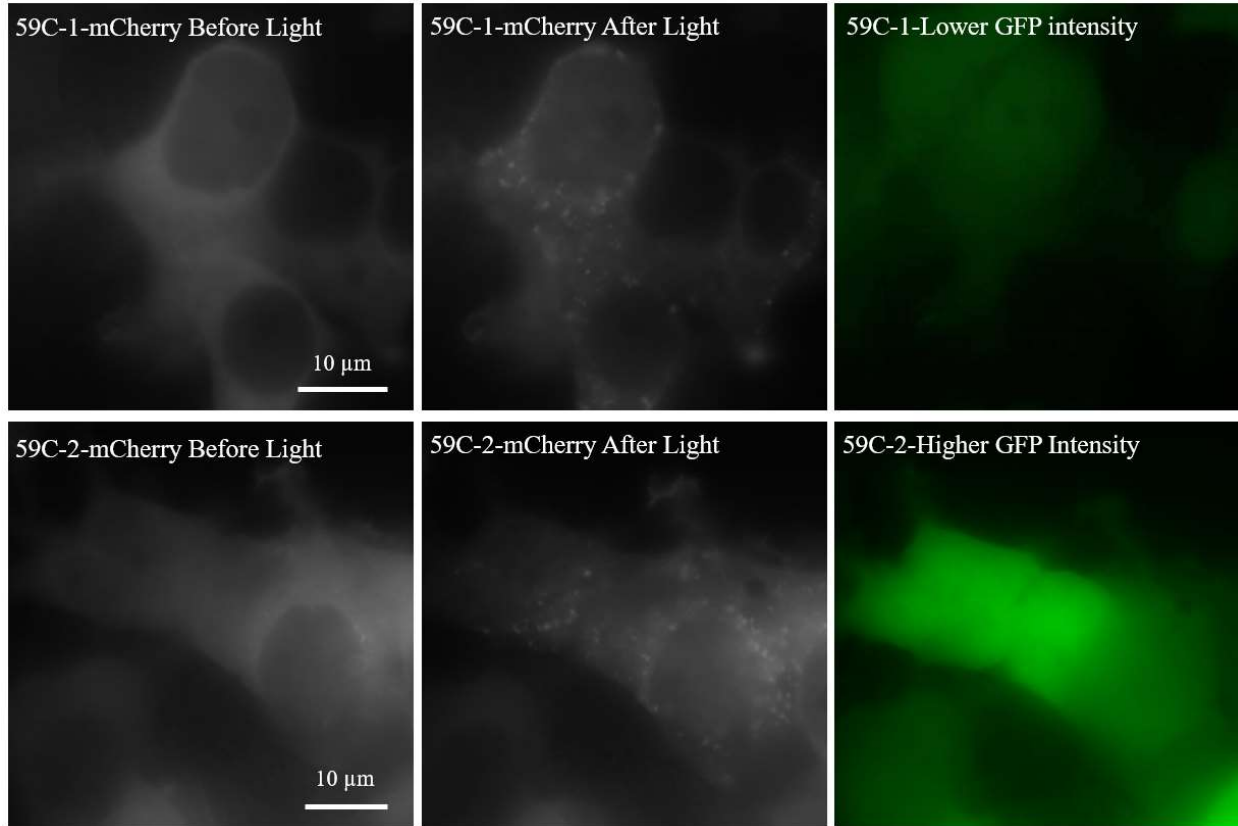
Figure 31: Optogenetic Cofilin Peptide expt; 59C
Leica widefield microscope images; Peptide transfection optogenetic experimentation, 59C fragment transfected HEK 293T cells under energetic stress conditions. From left to right, top to bottom; mCherry channel (Grey) before and after light exposure and a GFP transfection affirmation (Green) with a lower and higher GFP intensity respectively.

For the optogenetic experiments, the successfully transfected cells, cells that exhibited clusters, clusters per cell and relative GFP intensity were recorded to compare the fragments and their cluster inhibition properties. Interestingly, number of cells with clusters for the Long and 59N fragment weren't much different from the control where, when a cell that was transfected with the fragment exhibited clusters, the number of cells were at or around the same number that we could observe in the control cells. However, the 59C fragment showed a lower percentage of cells exhibiting clusters that was statistically significant as compared to the control shown in the bar graph in **Figure 32**. To better compare the experiments, as there was a noticeable difference

between transfected cells and control cells, the cells were counted using ImageJ's auto counting system where it narrows the relative intensity threshold of the image before light exposure and compares it to the same cell set after the 10-minute duration. The clusters per cell were then counted based on a pixel density from 20-200 and plotted against the normalized GFP intensity of the counted cells. The results of which are found in **Figures 33-35**.

Optogenetic Cluster Formation in Peptide Treated Cells
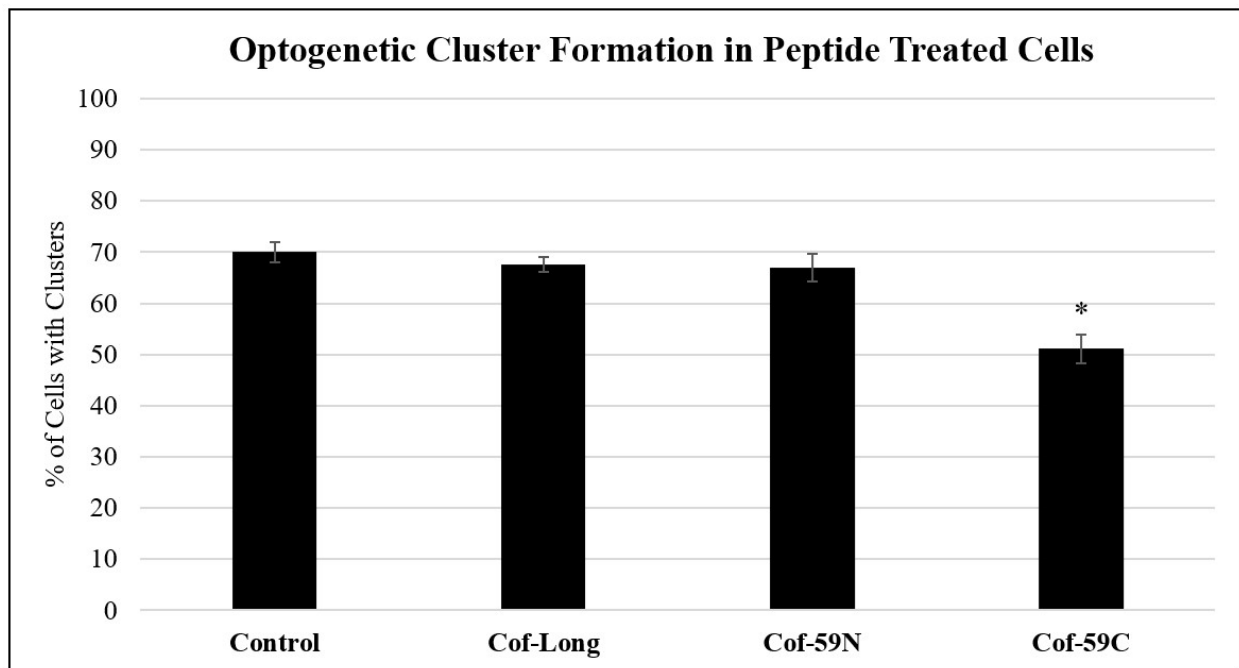
Figure 32: Optogenetic Cluster formation in Peptide Treated Cells
Bar graph illustrating the % of cells with clusters of HEK 293T cells under energetic stress conditions with a stressed control and transfected with the Long, 59N and 59C fragments. Each experiment had a n=50 cells where Cof-59C was statistically significant ($p < 0.05$) compared to the control using a one-way ANOVA.

The 59N fragment becomes obviously less efficient in decreasing the number of clusters per cell. When normalized to GFP intensity, the Long and 59C fragment experiments behave more similarly to each other in terms of average cluster per cell ratio. Where not as clear in the bar graph, **Figures 33-35** show more of a similar trend between the long and 59C fragment experiments as we seen a more negative trend as GFP intensity increases compared to the 59N fragment. More data points may need to be collected for these experiments as many cells with

intermediate clusters per cell/GFP intensity ratio were absent in both the long and 59C experiments

which may have been crucial to theory that these two fragments do in fact inhibit cluster formation.
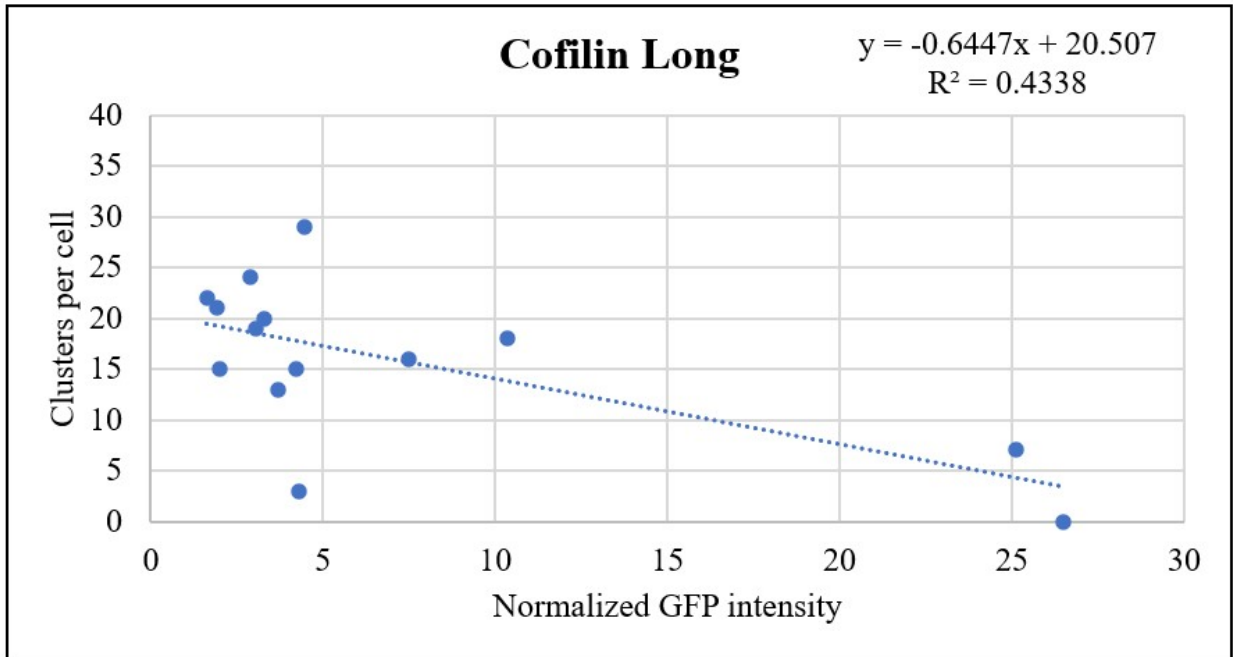
Figure 33: Normalized GFP Intensity vs. Clusters Per cell; Long
Scatter plot of Long fragment experiment. Plotted Normalized GFP intensity in successfully transfected cells to the clusters of the cell. n=14 cells counted and GFP intensity calculated.
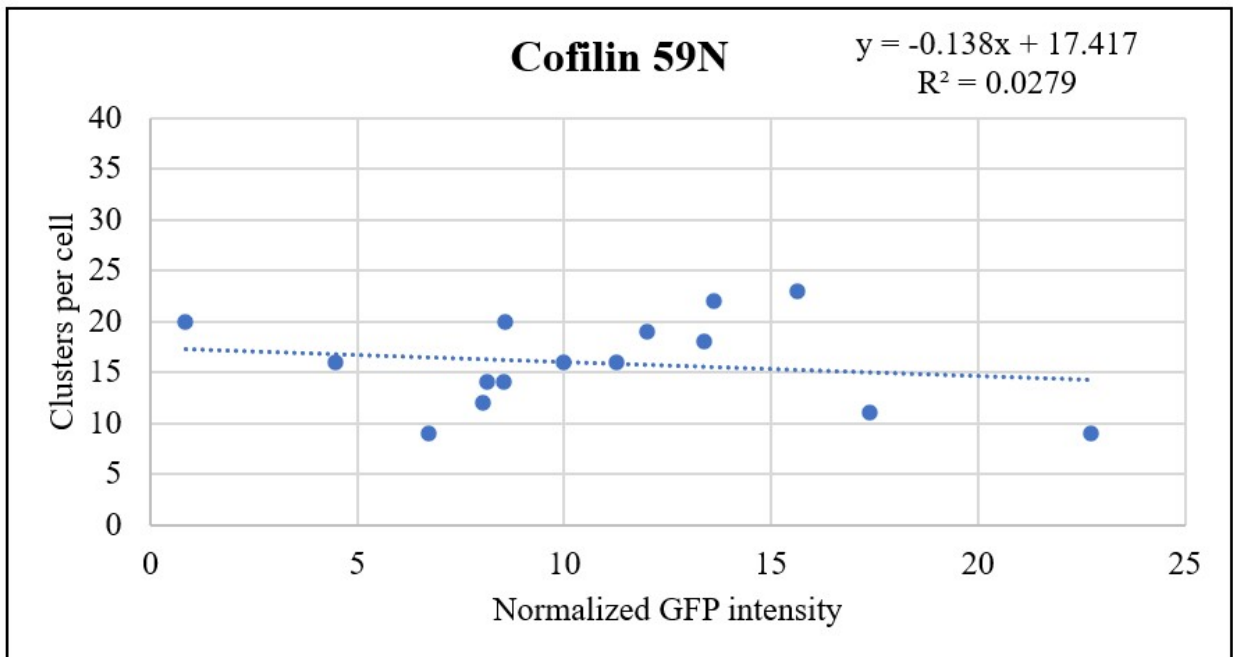
Figure 34: Normalized GFP Intensity vs. Clusters Per cell; 59N
Scatter plot of 59N fragment experiment. Plotted Normalized GFP intensity in successfully transfected cells to the clusters of the cell. n=15 cells counted and GFP intensity calculated.
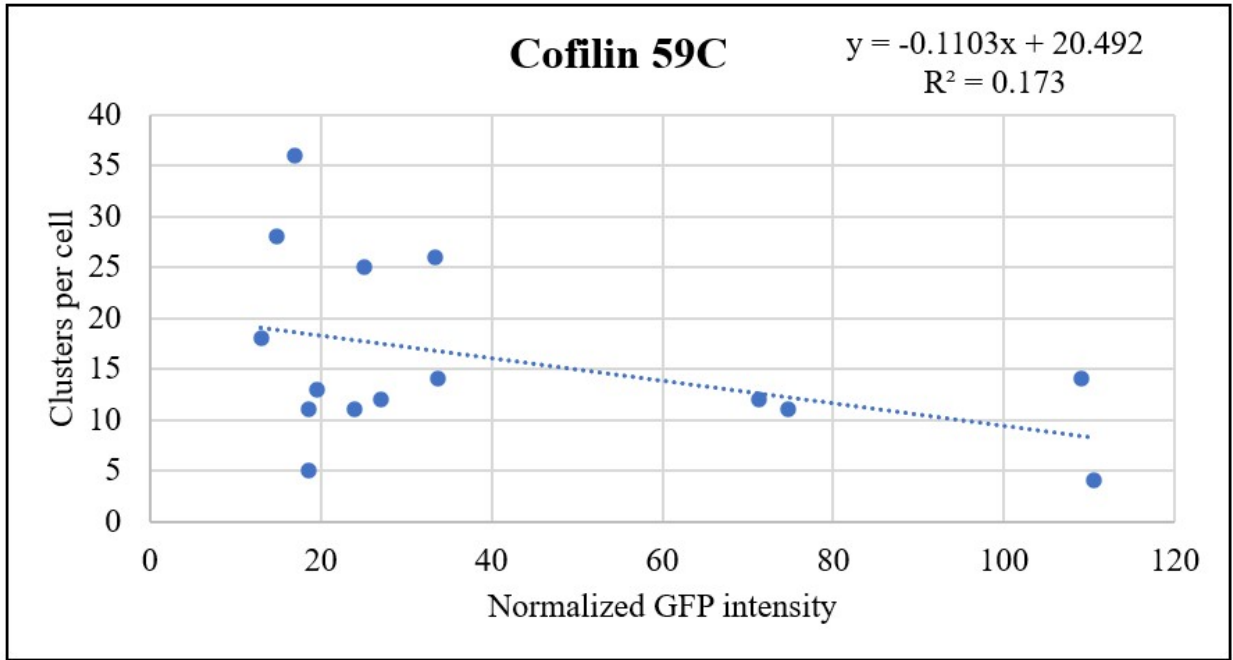
Figure 35: Normalized GFP Intensity vs. Clusters Per cell; 59C
Scatter plot of 59C fragment experiment. Plotted Normalized GFP intensity in successfully transfected cells to the clusters of the cell. n=15 cells counted and GFP intensity calculated.

Chapter 7: G-Binding Site Peptide Investigation and Amino Acid Mutations

Once the initial experiments were conducted, the results from the localization and optogenetic experiments lead to the investigation of the Long and the 59C fragment as they showed the most potential as inhibitory/ localization peptides respectively. The first stage of the investigation involved screening cells treated with different mutant variants of a smaller peptide variant, henceforth known as "COFPEP". We emphasized the amino acids associated with the G-binding site to actin as it shares a similar structure to the available LifeAct actin-localizing peptide as mentioned before. Below is a table with representing the observed interactions with actin under non-stressed conditions where COFPEP and its mutant variants were transfected into HeLa cells. **Table 4 and 5** shows the primers for COFPEP and its variants, the amino acid sequence with the areas highlighted in yellow (10), purple (11), and green (12) as the amino acids that were mutated at some point during the experiment and whether the transfected variant was actin-localized, mitochondria-localized, or showed no evidence of any localization. You can clearly see the actin localization from the LifeAct control in **Figure 36** but as mentioned before, using LifeAct as an actin-localization peptide can cause unwanted artifacts and effect actin dynamics in an undesirable way. There is promising actin localization in A11L, S, V, and Y where A11L and A11S are the most abundant. When moving onto the next phase, we compared the Long, 59C fragment with its original amino acid sequence along with the A11L and A11S variants, and the new COFPEP peptide with just the A11L and A11S variants.

Table 4: COFPEP Mutation Primers
COFPEP Primers based on the phCMV-NGFP vector (**Figure 19**) changed based on their relative amino acid mutation.

COFPEP Primers	Forward / Reverse
COFPEP-Native	TTAACAGAT CTCGAG ATG AAC GCC CCC CTG AAA TCT AAA ATG ATC TAT GCT TCG AGC AAG AATTCG AAGCTT CG GCTGCCGCC AAG TTT CTT CTT GAT CGC GTC CTT GCT CGA AGC ATA
S12F	TTAACAGAT CTCGAG ATG AAC GCC CCC CTG AAA TCT AAA ATG ATC TAT GCT TTT AGC AAG AATTCG AAGCTT CG GCTGCCGCC AAG TTT CTT CTT GAT CGC GTC CTT GCT AAA AGC ATA
S12W	TTAACAGAT CTCGAG ATG AAC GCC CCC CTG AAA TCT AAA ATG ATC TAT GCT TGG AGC AAG AATTCG AAGCTT CG GCTGCCGCC AAG TTT CTT CTT GAT CGC GTC CTT GCT CCA AGC ATA
YAS-KKF	TTAACAGAT CTCGAG ATG AAC GCC CCC CTG AAA TCT AAA ATG ATC AAA AAG TTC AGC AAG AATTCG AAGCTT CG GCTGCCGCC AAG TTT CTT CTT GAT CGC GTC CTT GCT GAA CTT TTT
A11F	TTAACAGAT CTCGAG ATG AAC GCC CCC CTG AAA TCT AAA ATG ATC TAT TTT TCG AGC AAG AATTCG AAGCTT CG GCTGCCGCC AAG TTT CTT CTT GAT CGC GTC CTT GCT CGA AAA ATA
A11L	TTAACAGAT CTCGAG ATG AAC GCC CCC CTG AAA TCT AAA ATG ATC TAT CTC TCG AGC AAG AATTCG AAGCTT CG GCTGCCGCC AAG TTT CTT CTT GAT CGC GTC CTT GCT CGA GAG ATA
A11S	TTAACAGAT CTCGAG ATG AAC GCC CCC CTG AAA TCT AAA ATG ATC TAT TCG TCG AGC AAG AATTCG AAGCTT CG GCTGCCGCC AAG TTT CTT CTT GAT CGC GTC CTT GCT CGA CGA ATA
A11V	TTAACAGAT CTCGAG ATG AAC GCC CCC CTG AAA TCT AAA ATG ATC TAT GTT TCG AGC AAG AATTCG AAGCTT CG GCTGCCGCC AAG TTT CTT CTT GAT CGC GTC CTT GCT CGA AAC ATA
A11Y	TTAACAGAT CTCGAG ATG AAC GCC CCC CTG AAA TCT AAA ATG ATC TAT TAT TCG AGC AAG AATTCG AAGCTT CG GCTGCCGCC AAG TTT CTT CTT GAT CGC GTC CTT GCT CGA ATA ATA

Table 5: COFPEP Mutant variants Localization Patterns
COFPEP Peptide mutations and localization under non-stress conditions. Amino acids 10, 11 and 12 are highlighted in yellow, purple, and green respectively. These amino acids were shown to be key factors in the G-binding site of cofilin to actin. The peptide was derived from the native amino acid sequence of cofilin with reference from the previously generated 59C fragment.

COFPEP M-NAPLKSKMIYASSKDAIKKKL	Localization		
	Actin	Mitochondrial	None
LifeAct Control	X		
Native 12S COFPEP			X
A12F			X
A12W		X	
A10,11,12-KKF	slight		
A11F	slight		
A11L	X		
A11S	X		
A11V	X		
A11Y	X		
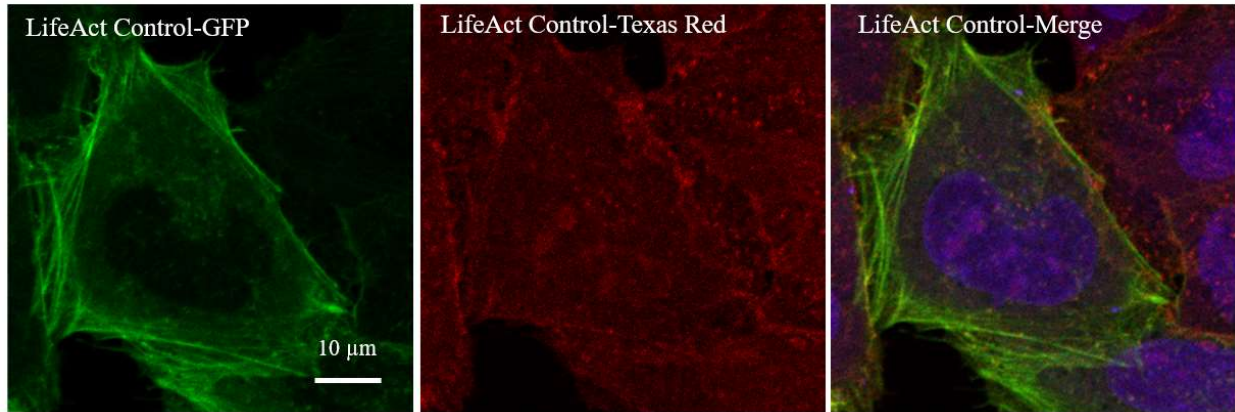
Figure 36: COFPEP Mutant Variant expt; LifeAct Control
Zeiss 700 Confocal microscope images; Native actin localization experimentation. LifeAct Peptide control under non-stressed conditions (from left to right) GFP channel (Green), Texas Red channel (Red), and Overlay (GFP, Texas Red, DAPI (Blue)).
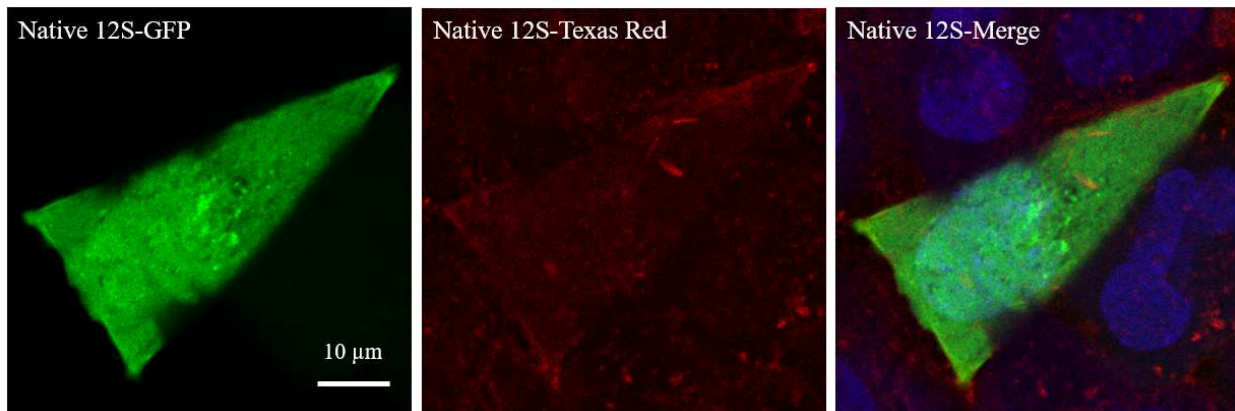
Figure 37: COFPEP Mutant Variant expt; Native 12S
Zeiss 700 Confocal microscope images; Native actin localization experimentation. Native 12S peptide under non-stressed conditions (from left to right) GFP channel (Green), Texas Red channel (Red), and Overlay (GFP, Texas Red, DAPI (Blue)).

Figure 38: COFPEP Mutant Variant expt; 12F Mutation
Zeiss 700 Confocal microscope images; Native actin localization experimentation. 12F mutation peptide under non-stressed conditions (from left to right) GFP channel (Green), Texas Red channel (Red), and Overlay (GFP, Texas Red, DAPI (Blue)).

Figure 39: COFPEP Mutant Variant expt; 12W Mutation
Zeiss 700 Confocal microscope images; Native actin localization experimentation. 12W mutation peptide under non-stressed conditions (from left to right) GFP channel (Green), Texas Red channel (Red), and Overlay (GFP, Texas Red, DAPI (Blue)).

Figure 40: COFPEP Mutant Variant expt; YAS-KKF Mutation
Zeiss 700 Confocal microscope images; Native actin localization experimentation. $Y_{10}A_{11}S_{12}$-KKF mutation peptide under non-stressed conditions (from left to right) GFP channel (Green), Texas Red channel (Red), and Overlay (GFP, Texas Red, DAPI (Blue)).
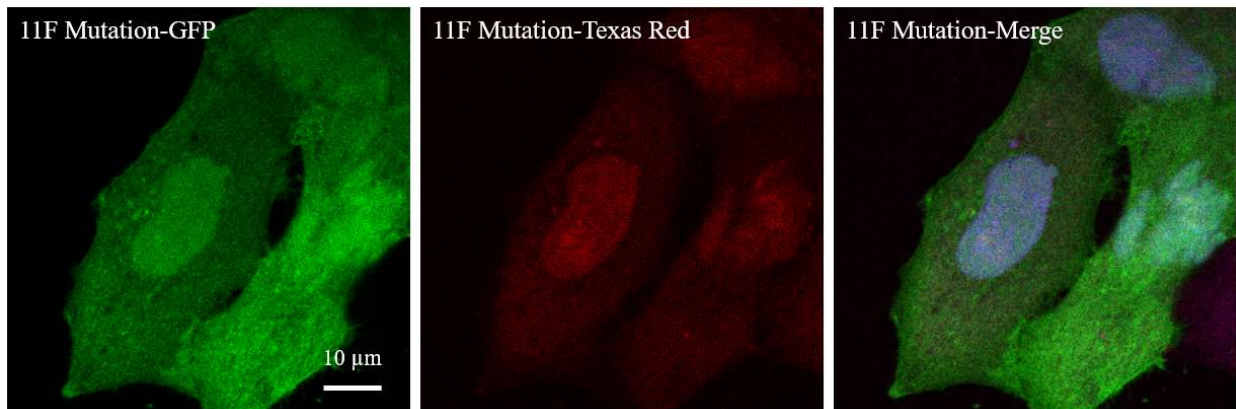
Figure 41: COFPEP Mutant Variant expt; 11F Mutation
Zeiss 700 Confocal microscope images; Native actin localization experimentation. 11F mutation peptide under non-stressed conditions (from left to right) GFP channel (Green), Texas Red channel (Red), and Overlay (GFP, Texas Red, DAPI (Blue)).
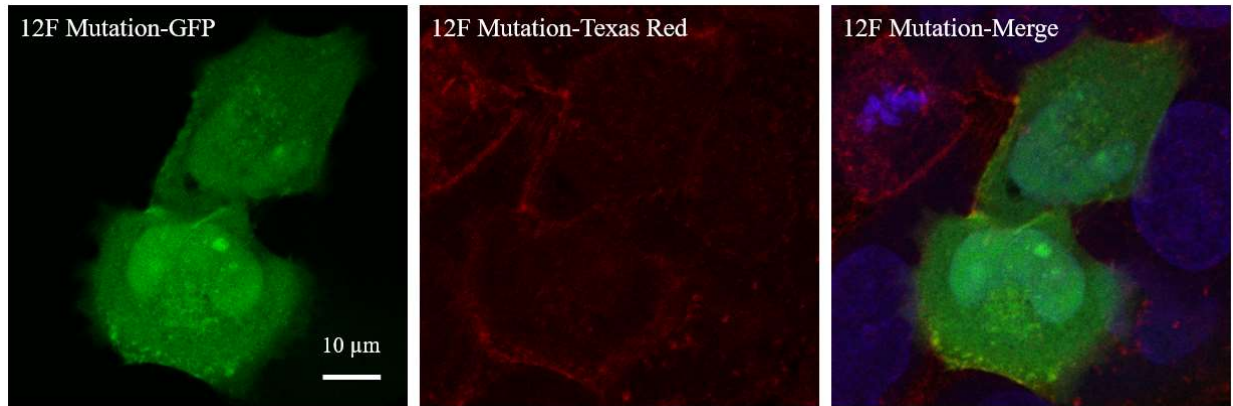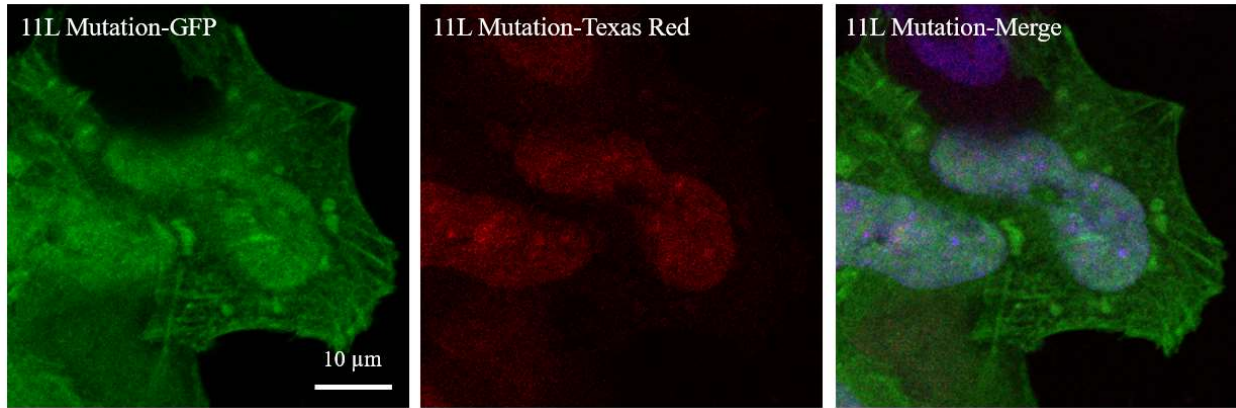
Figure 42: COFPEP Mutant Variant expt; 11L Mutation
Zeiss 700 Confocal microscope images; Native actin localization experimentation. 11L mutation peptide under non-stressed conditions (from left to right) GFP channel (Green), Texas Red channel (Red), and Overlay (GFP, Texas Red, DAPI (Blue)).
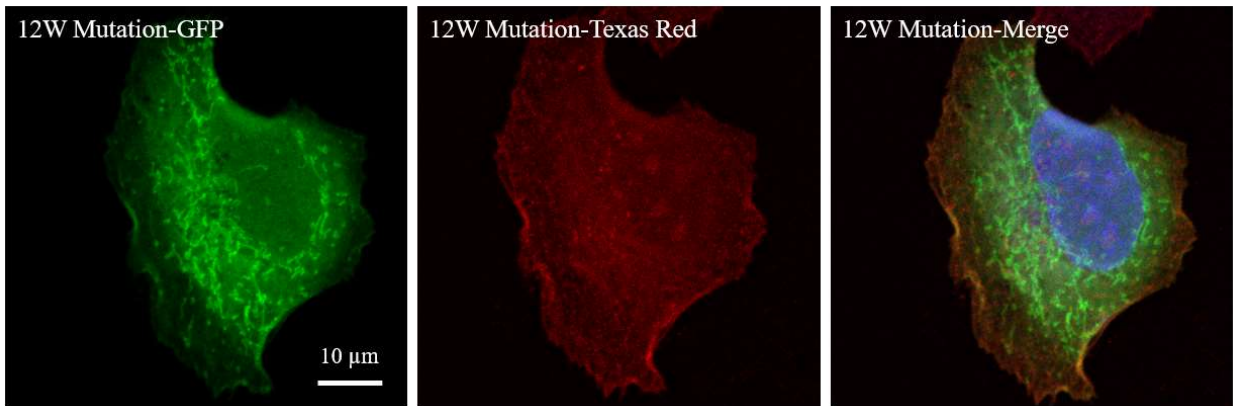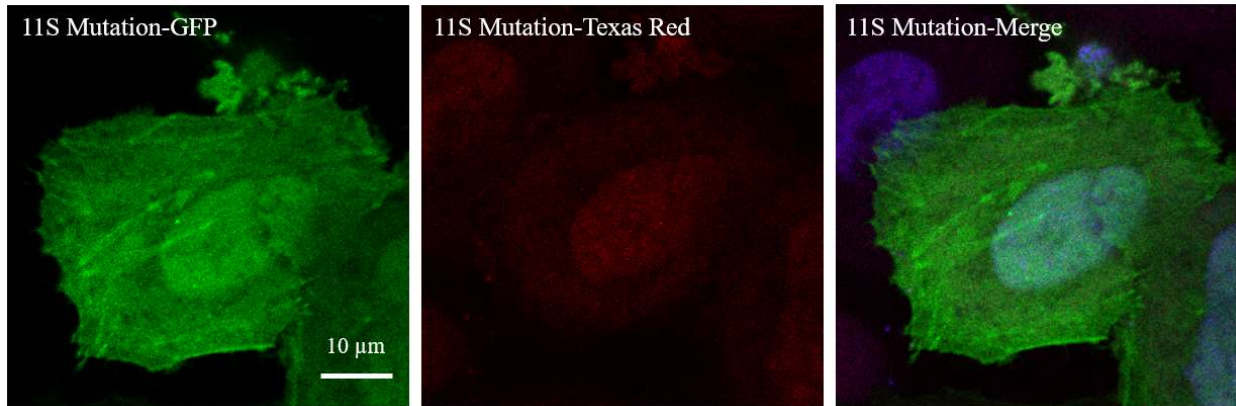

Figure 43: COFPEP Mutant Variant expt; 11S Mutation
Zeiss 700 Confocal microscope images; Native actin localization experimentation. 11S mutation peptide under non-stressed conditions (from left to right) GFP channel (Green), Texas Red channel (Red), and Overlay (GFP, Texas Red, DAPI (Blue)).
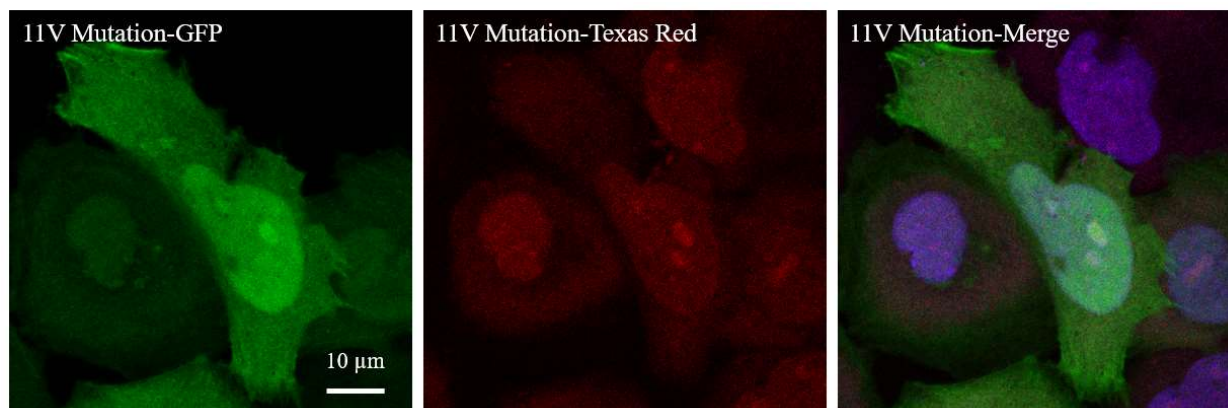
Figure 44: COFPEP Mutant Variant expt; 11V Mutation
Zeiss 700 Confocal microscope images; Native actin localization experimentation. 11V mutation peptide under non-stressed conditions (from left to right) GFP channel (Green), Texas Red channel (Red), and Overlay (GFP, Texas Red, DAPI (Blue)).
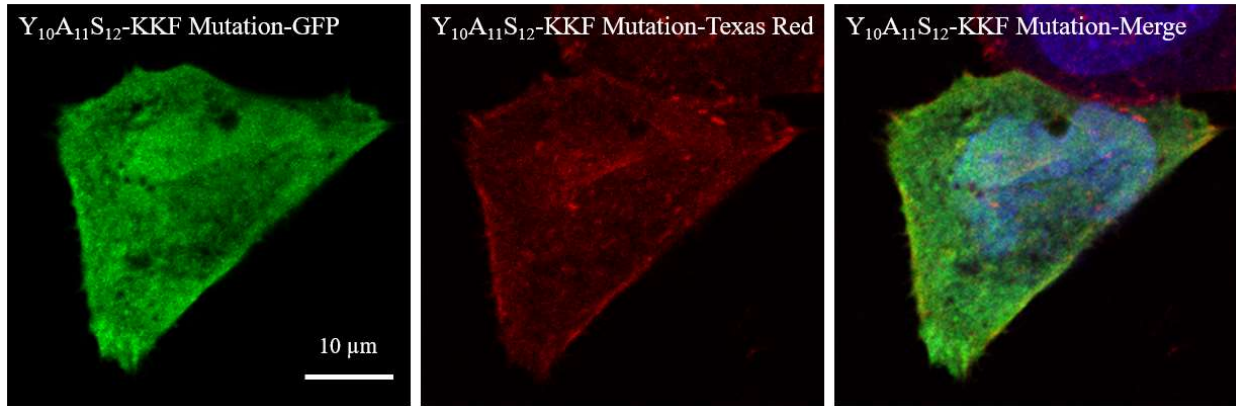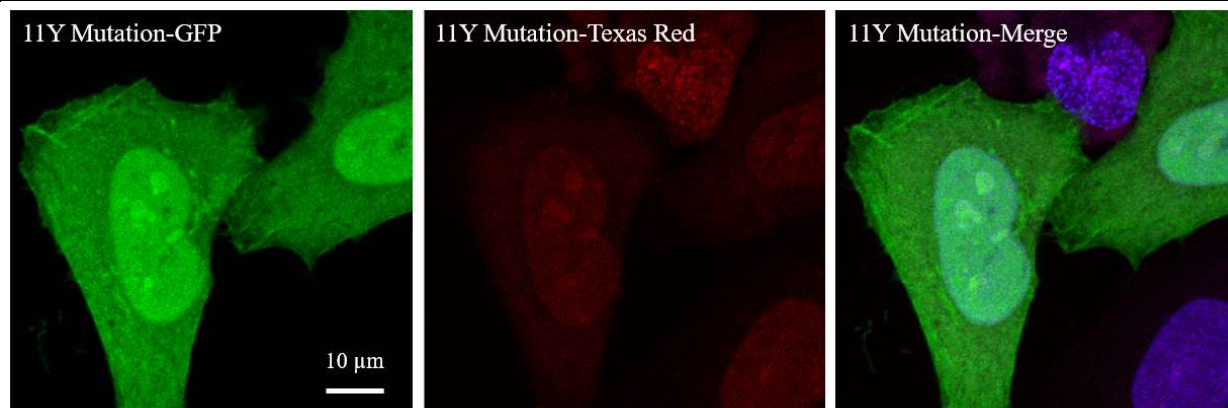

Figure 45: COFPEP Mutant Variant expt; 11Y Mutation
Zeiss 700 Confocal microscope images; Native actin localization experimentation. 11Y mutation peptide under non-stressed conditions (from left to right) GFP channel (Green), Texas Red channel (Red), and Overlay (GFP, Texas Red, DAPI (Blue)).

After we found that the new COFPEP A11L and A11S variants exhibited strong actin localization under non stress conditions, we decided to test these peptides under stress conditions and compare the inhibition/ actin-localization properties. This experiment was done without the optogenetic proteins as we were only looking at the peptides' natural ability to inhibit actin-cofilin rod formation. At first, the experiment was imaged on the Zeiss 700 confocal microscope. However, it was difficult to determine an accurate rod count while looking through the planes of

61

the Z-stack system. Therefore, the cells were re-imaged on the Leica widefield microscope to obtain cell images that would allow for a more accurate rod per cell calculation when quantifying the data. Looking back at the previous COFPEP experiments, we also noticed that treatment with these peptides made it difficult to observe the Texas Red actin stain that we had originally used during the immunostaining process. When these experiments were conducted, we switched to an Alexa 568 immunostain which worked much better in viewing the actin-cofilin rods as well as had a much better fluorescence. Upon closer inspection of the cell images (**Figures 46-52**), the actin-cofilin rods are clearly present in the control cells as many of the cells had multiple rods per cell with an average length of more than 4 µm. However, at first glance, the peptide-transfected cells do not seem to exhibit any significant rods. Upon closer examination, the peptide treated cells had lower rods per cell as well as a much smaller average rod size where some were even less than 2 µm long. When comparing all the peptide-transfected cells to the control (**Figure 53**), all conditions were statistically significant compared to the control ($p < 0.05$; one-way ANOVA). Average rod size in the 59C, and the A11S variants of both the 59C fragment and the COFPEP peptide were around 3 µm long, where the COFPEP A11S variant was the shortest of the three. What is really promising is that the Long fragment, and both the 59C and COFPEP A11L variants all exhibited a very small average rod size at or lower than 2 µm meaning that it is possible these peptides are the most effective at inhibiting the formation of actin-cofilin rods during energetic stress conditions.
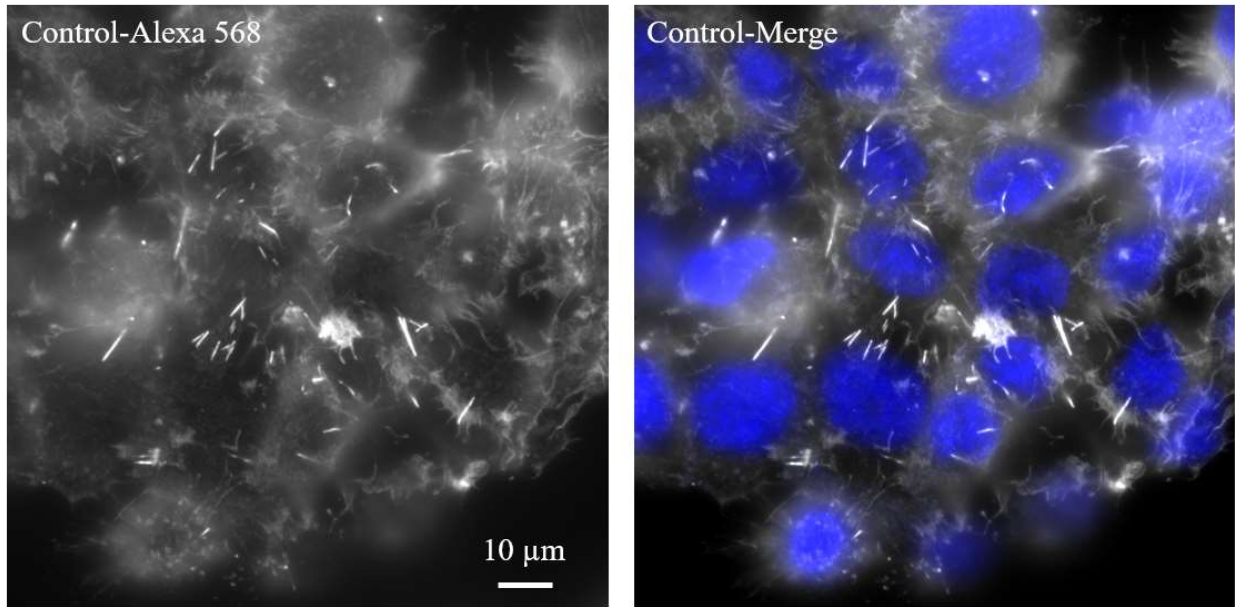
Figure 46: Cofilin Peptide and COFPEP Stress Condition expt; Control
Leica widefield microscope images; Peptide-Actin localization under stress conditions, Control, 1hr under energetic stress conditions (4.8 µL; 0.625 M sodium azide: 0.375 M DDG). From left to right, Alexa 568 channel (Grey) and Merge channels (Alexa 568 & DAPI (Blue)).
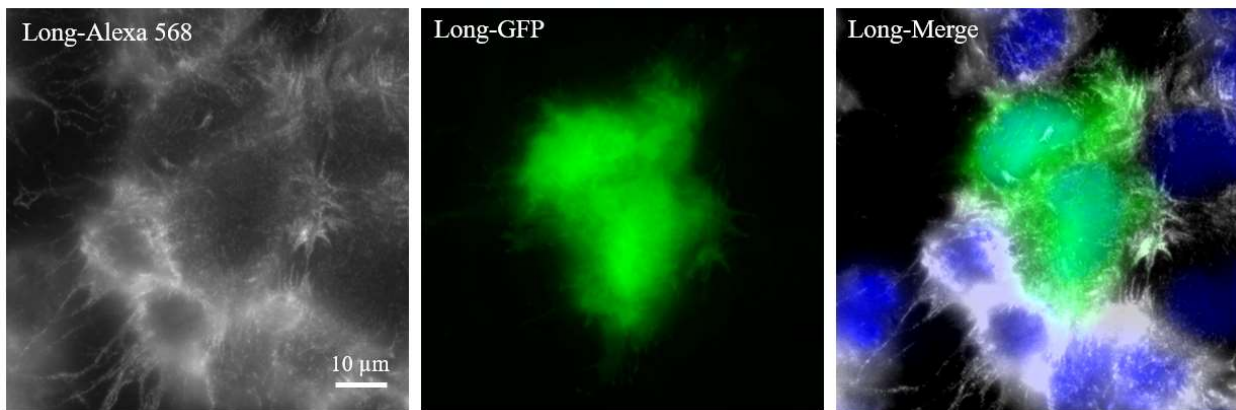
Figure 47: Cofilin Peptide and COFPEP Stress Condition expt; Long
Leica widefield microscope images; Peptide-Actin localization under stress conditions, Long Fragment, 1hr under energetic stress conditions (4.8 µL; 0.625 M sodium azide: 0.375 M DDG). From left to right, Alexa 568 channel (Grey), GFP channel (Green), and Merge channels (Alexa 568, GFP & DAPI (Blue)).

Figure 48: Cofilin Peptide and COFPEP Stress Condition expt; 59C
Leica widefield microscope images; Peptide-Actin localization under stress conditions, 59C Fragment, 1hr under energetic stress conditions (4.8 µL; 0.625 M sodium azide: 0.375 M DDG). From left to right, Alexa 568 channel (Grey), GFP channel (Green), and Merge channels (Alexa 568, GFP & DAPI (Blue)).

Figure 49: Cofilin Peptide and COFPEP Stress Condition expt; 59C-A11L
Leica widefield microscope images; Peptide-Actin localization under stress conditions, 59C 11L mutation, 1hr under energetic stress conditions (4.8 µL; 0.625 M sodium azide: 0.375 M DDG). From left to right, Alexa 568 channel (Grey), GFP channel (Green), and Merge channels (Alexa 568, GFP & DAPI (Blue)).
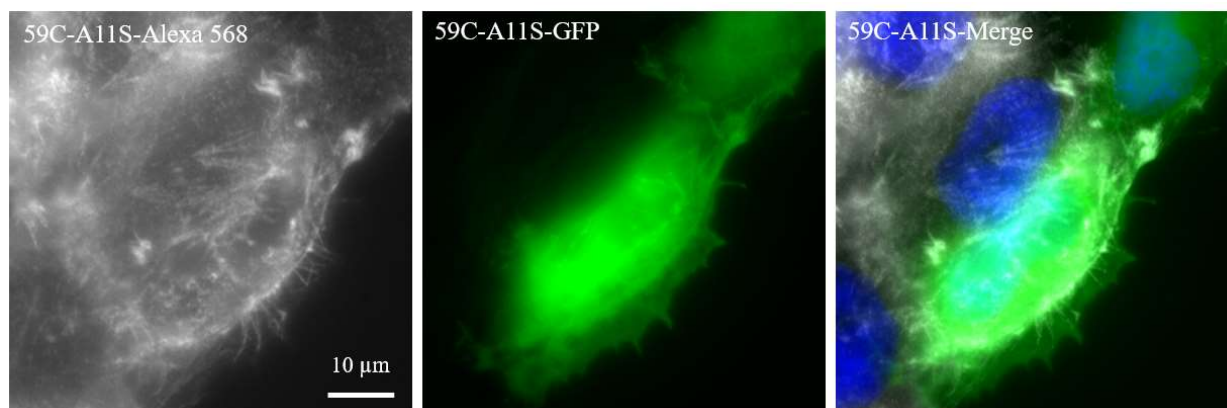
Figure 50: Cofilin Peptide and COFPEP Stress Condition expt; 59C-A11S
Leica widefield microscope images; Peptide-Actin localization under stress conditions, 59C 11S mutation, 1hr under energetic stress conditions (4.8 µL; 0.625 M sodium azide: 0.375 M DDG). From left to right, Alexa 568 channel (Grey), GFP channel (Green), and Merge channels (Alexa 568, GFP & DAPI (Blue)).
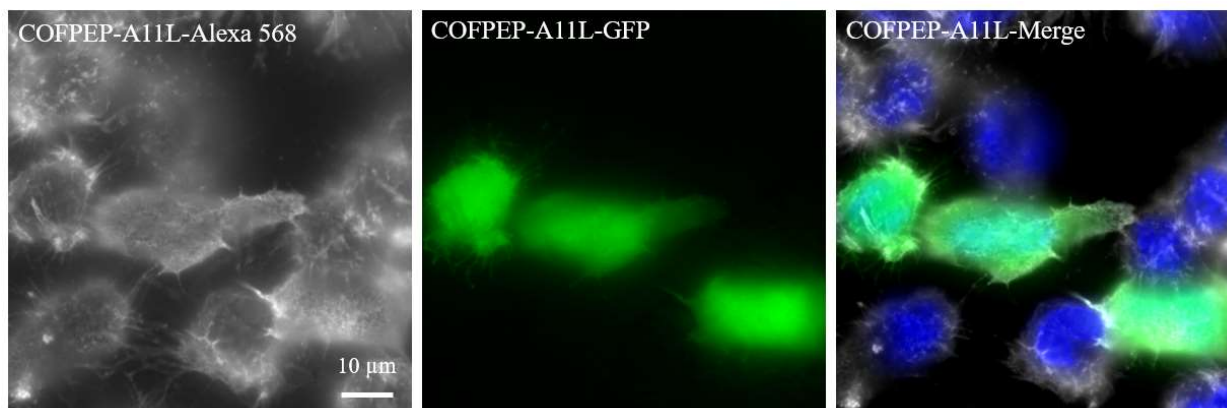
Figure 51: Cofilin Peptide and COFPEP Stress Condition expt; COFPEP-A11L
Leica widefield microscope images; Peptide-Actin localization under stress conditions, COFPEP 11L mutation, 1hr under energetic stress conditions (4.8 µL; 0.625 M sodium azide: 0.375 M DDG). From left to right, Alexa 568 channel (Grey), GFP channel (Green), and Merge channels (Alexa 568, GFP & DAPI (Blue)).
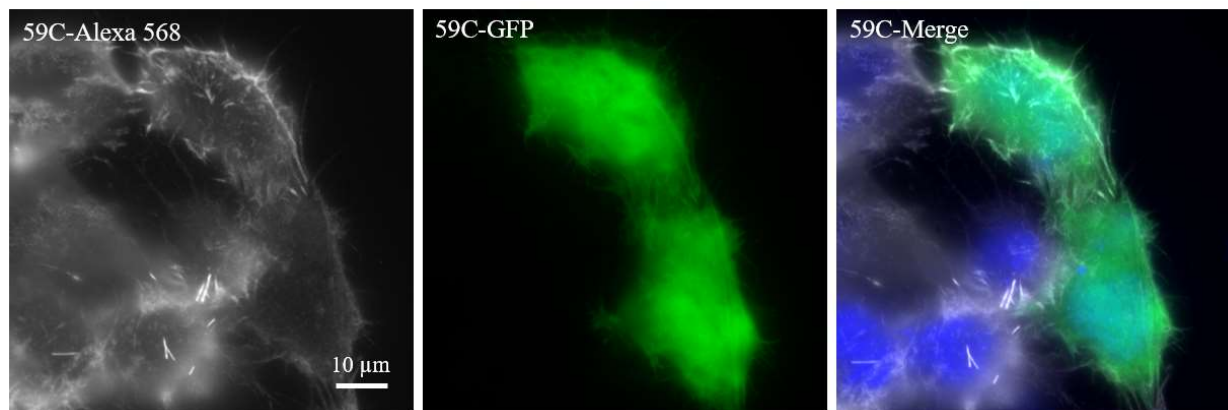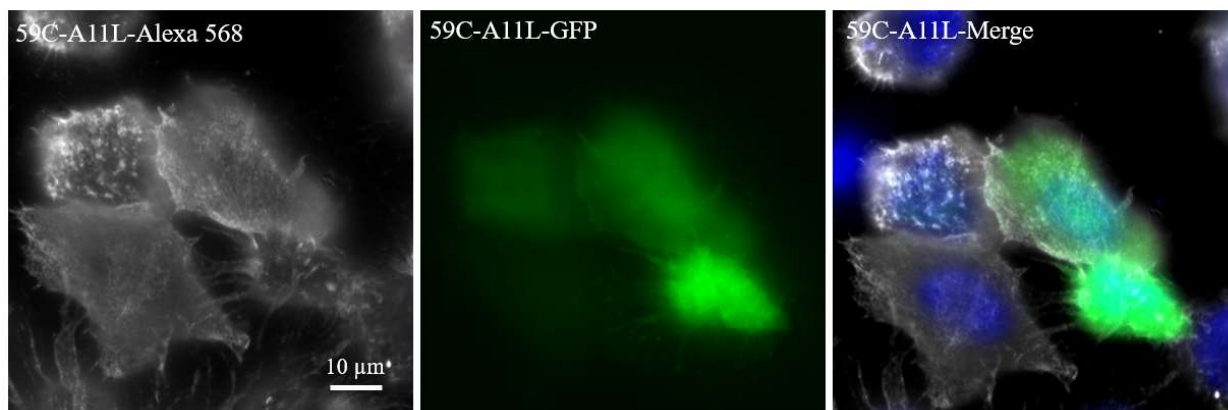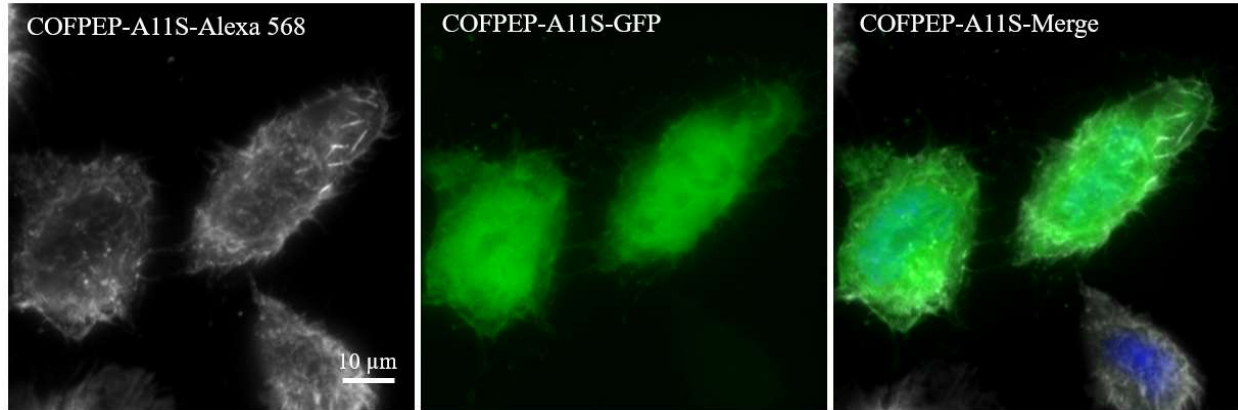
Figure 52: Cofilin Peptide and COFPEP Stress Condition expt; COFPEP-A11S
Leica widefield microscope images; Peptide-Actin localization under stress conditions, COFPEP 11S mutation, 1hr under energetic stress conditions (4.8 µL; 0.625 M sodium azide: 0.375 M DDG). From left to right, Alexa 568 channel (Grey), GFP channel (Green), and Merge channels (Alexa 568, GFP & DAPI (Blue)).
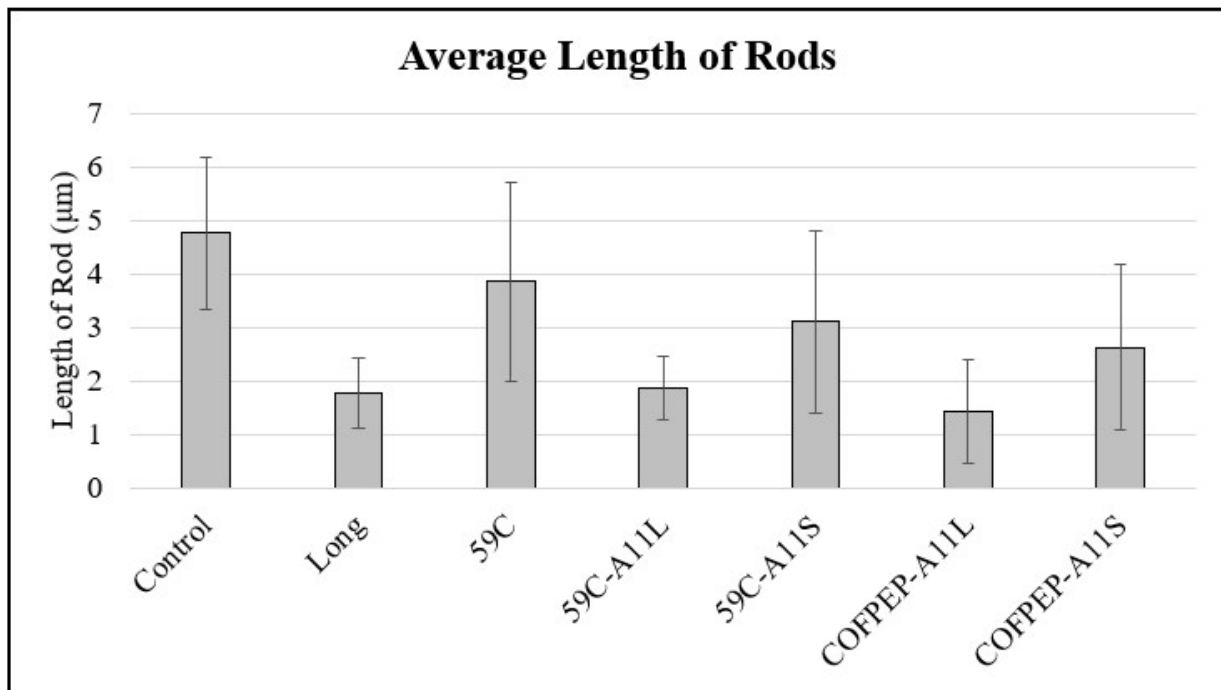
Figure 53: Average Length of Actin-Cofilin rods in Peptide/ COFPEP Treated Cells
Bar graph comparing the average length of actin-cofilin rods in HeLa cells transfected with the Long, 59C (original, 11L &11S mutations) and COFPEP peptides (11L &11S mutations). Where n=10 cells per condition and all samples were statistically significant ($p < 0.05$) to the control condition via a one-way ANOVA.

Chapter 8:   Discussion and Conclusions

Ultimately there are many things that go unanswered from what we have found in this research. The results that we accumulated during both main topics in the research each gave some promising answers to actin rod inhibition with the added actin localization efficiency of some of the created peptides and their variants. The nonhydrolyzable ATP experiments did not have the expected outcome that we had originally hypothesized once the results from the concentrations titration was quantified. Optogenetically, the ATP analogues didn't have the anticipated reaction with the CofActor system that was introduced. This led to the idea that perhaps we are blocking necessary cell ion channels that were ATP dependent with the nonhydrolyzable analogues that which caused an influx in the cluster formation at different concentrations. Literature states that the P2X receptor has at least 3 molecules of ATP on the extracellular portion of the open P2X channels meaning that the nonhydrolyzable ATP analogues may be blocking the P2 receptors from opening.[42] More work could be done to investigate what the main effects of the addition of the nonhydrolyzable ATP analogues are and bring light to pathways that may be more beneficial to actin-cofilin rod inhibition that have not been explored yet. The most promising aspect of this research is the potential that the cofilin peptides have as actin-cofilin rod inhibitors/ actin localizers. Recalling the peptide mutations and the more in-depth work with the G- binding site and COFPEP, these peptides may have a place in the market as a potential competitor to LifeAct without the unwanted artifacts that we have seen when using this actin-localizing peptide. More specifically, the A11 mutations from the G-binding site within the COFPEP and 59C fragment shows promise as this residue has shown to have some impact in native cofilin binding to F-actin.[43] As for the results from the native rod inhibition, the Long fragment may be a promising candidate for future variants as it resembles the data from the A11L variants of the 59C fragment and the

COFPEP peptide. What is most interesting is that it has the same effect as these variants but is ultimately from a different binding site to actin (F-site). The introduction of the optogenetic CofActor system to the peptide investigation left room for improvements as the number of clusters per cell indicated that the long and 59C fragments may be inhibiting the formation of the optogenetic clusters. After immunostaining the new peptides within the cells, we noticed that the Texas Red stain that we used was give fewer effective results in terms of observing actin localization. This could be due to interference from the peptides or a bad reagent but when looking at the light range of Texas Red, the range is much smaller than other fluorescent proteins which may be why we started to see a decrease in fluorescent response.[44] When moving to Alexa 568, it acts more similar to mCherry which we have seen to be a more effective fluorescent protein based on some of our previous experiments. The mutant variants of the 59C fragment and COFPEP peptide may also show similar results. After investigating the localization of the COFPEP and the Cof-Long and 59C fragments, it is essential that we investigate the localization of native Cofilin-1 in the Hela and HEK 293T cell lines to ensure that we are localizing to actin and not interrupting actin dynamics in any way. It is shown in the literature that native cofilin and overactive variants such as the S3ECofilin used in this research exhibit localization patterns to actin under stress conditions different from the ones that were seen in this research.[45,46] Native cofilin-1 localization may be used as a control to observe any changes to the localization and/ or actin dynamics.

Implementing the CofActor system to the Long, 59C, and COFPEP peptide may be an experiment that is conducted in the future once a library of suitable variants of the three have been screened. There is already an experiment underway that involves the CIB/ Cry2 system where the CofilinS3E-Cry2-mCherry will be introduced to a PEPTIDE-CIB-GFP treated cell where we try to recruit cofilin to actin and observe any changes to the actin bound peptides. Current research at

the Brody School of Medicine is looking into the peptides' morphological characterization and introducing these constructs into untested biological instrumentation such as FRAP, and STORM super-resolution imaging of actin bundles. Using other microscope techniques such as FRAP; we could even learn more about the mobilities of these peptides within the cell lines.[47] In the future, there might be a way to introduce these peptides and small molecules into clinical research scenarios so that they can screen for therapeutics that may be beneficial for actin-cofilin rod depolymerization or inhibition which can be seen as a way to treat patients with early signs of AD.

References

(1)   Bamburg, J. R.; Bernstein, B. W. Actin Dynamics and Cofilin-Actin Rods in Alzheimer Disease. *Cytoskeleton* **2016**, *73* (9), 477–497. https://doi.org/10.1002/cm.21282.

(2)   Penzes, P.; VanLeeuwen, J.-E. Impaired Regulation of Synaptic Actin Cytoskeleton in Alzheimer's Disease. *Brain Res. Rev.* **2011**, *67* (1–2), 184–192. https://doi.org/10.1016/J.BRAINRESREV.2011.01.003.

(3)   Lane, C. A.; Hardy, J.; Schott, J. M. Alzheimer's Disease. *European Journal of Neurology*. Blackwell Publishing Ltd January 1, 2018, pp 59–70. https://doi.org/10.1111/ene.13439.

(4)   Prince, M.; Albanese, E.; Pender, R.; Ferri, C.; Mazzotti, D. R.; Piovezan, R. D.; Padilla, I.; Luchsinger, J. A. World Alzheimer Report 2014 Dementia and Risk Reduction AN ANALYSIS OF PROTECTIVE AND MODIFIABLE FACTORS SUPPORTED BY Dr Maëlenn Guerchet Dr Matthew Prina. **2014**.

(5)   Jonsson, T.; Atwal, J. K.; Steinberg, S.; Snaedal, J.; Jonsson, P. V; Bjornsson, S.; Stefansson, H.; Sulem, P.; Gudbjartsson, D.; Maloney, J.; Hoyte, K.; Gustafson, A.; Liu, Y.; Lu, Y.; Bhangale, T.; Graham, R. R.; Huttenlocher, J.; Bjornsdottir, G.; Andreassen, O. A.; Jönsson, E. G.; Palotie, A.; Behrens, T. W.; Magnusson, O. T.; Kong, A.; Thorsteinsdottir, U.; Watts, R. J.; Stefansson, K. A Mutation in APP Protects against Alzheimer's Disease and Age-Related Cognitive Decline. *Nature* **2012**. https://doi.org/10.1038/nature11283.

(6)   Bernstein, B. W.; Shaw, A. E.; Minamide, L. S.; Pak, C. W.; Bamburg, J. R. Incorporation of Cofilin into Rods Depends on Disulfide Intermolecular Bonds: Implications for Actin Regulation and Neurodegenerative Disease. *J. Neurosci.* **2012**, *32* (19), 6670. https://doi.org/10.1523/JNEUROSCI.6020-11.2012.

(7)   Rost, B. R.; Schneider-Warme, F.; Schmitz, D.; Hegemann, P. Optogenetic Tools for Subcellular Applications in Neuroscience. *Neuron* **2017**, *96* (3), 572–603. https://doi.org/10.1016/J.NEURON.2017.09.047.

(8)   Jiang, J.; Cui, H.; Rahmouni, K. Optogenetics and Pharmacogenetics: Principles and Applications. *Am. J. Physiol. Integr. Comp. Physiol.* **2017**, *313* (6), R633–R645. https://doi.org/10.1152/ajpregu.00091.2017.

(9)   Krueger, D.; Izquierdo, E.; Viswanathan, R.; Hartmann, J.; Cartes, C. P.; de Renzis, S. Principles and Applications of Optogenetics in Developmental Biology. *Dev.* **2019**, *146* (20). https://doi.org/10.1242/dev.175067.

(10)   Ozkan-Dagliyan, I.; Chiou, Y.-Y.; Ye, R.; Hassan, B. H.; Ozturk, N.; Sancar, A. Formation of Arabidopsis Cryptochrome 2 Photobodies in Mammalian Nuclei APPLICATION AS AN OPTOGENETIC DNA DAMAGE CHECKPOINT SWITCH *. **2013**. https://doi.org/10.1074/jbc.M113.493361.

(11) Jin, M.; Shepardson, N.; Yang, T.; Chen, G.; Walsh, D.; Selkoe, D. J. Soluble Amyloid β-Protein Dimers Isolated from Alzheimer Cortex Directly Induce Tau Hyperphosphorylation and Neuritic Degeneration. *Proc. Natl. Acad. Sci. U. S. A.* **2011**, *108* (14), 5819. https://doi.org/10.1073/PNAS.1017033108.

(12) Kametani, F.; Hasegawa, M. Reconsideration of Amyloid Hypothesis and Tau Hypothesis in Alzheimer's Disease. *Front. Neurosci.* **2018**, *12* (JAN). https://doi.org/10.3389/FNINS.2018.00025.

(13) Masters, C. L.; Simms, G.; Weinman, N. A.; Multhaup, G.; McDonald, B. L.; Beyreuther, K. Amyloid Plaque Core Protein in Alzheimer Disease and Down Syndrome. *Proc. Natl. Acad. Sci. U. S. A.* **1985**, *82* (12), 4245. https://doi.org/10.1073/PNAS.82.12.4245.

(14) Lambert, M. P.; Barlow, A. K.; Chromy, B. A.; Edwards, C.; Freed, R.; Liosatos, M.; Morgan, T. E.; Rozovsky, I.; Trommer, B.; Viola, K. L.; Wals, P.; Zhang, C.; Finch, C. E.; Krafft, G. A.; Klein, W. L. Diffusible, Nonfibrillar Ligands Derived from Aβ1–42 Are Potent Central Nervous System Neurotoxins. *Proc. Natl. Acad. Sci. U. S. A.* **1998**, *95* (11), 6448. https://doi.org/10.1073/PNAS.95.11.6448.

(15) Wang, J. Z.; Xia, Y. Y.; Grundke-Iqbal, I.; Iqbal, K. Abnormal Hyperphosphorylation of Tau: Sites, Regulation, and Molecular Mechanism of Neurofibrillary Degeneration. *Journal of Alzheimer's Disease*. IOS Press 2013. https://doi.org/10.3233/JAD-2012-129031.

(16) Metaxas, A.; Kempf, S. J. Neurofibrillary Tangles in Alzheimer's Disease: Elucidation of the Molecular Mechanism by Immunohistochemistry and Tau Protein Phospho-Proteomics. *Neural Regen. Res.* **2016**, *11* (10), 1579. https://doi.org/10.4103/1673-5374.193234.

(17) H, Z.; E, M. Lost after Translation: Missorting of Tau Protein and Consequences for Alzheimer Disease. *Trends Neurosci.* **2014**, *37* (12), 721–732. https://doi.org/10.1016/J.TINS.2014.08.004.

(18) Minamide, L. S.; Striegl, A. M.; Boyle, J. A.; Meberg, P. J.; Bamburg, J. R. Neurodegenerative Stimuli Induce Persistent ADF/Cofilin–Actin Rods That Disrupt Distal Neurite Function. *Nat. Cell Biol.* **2000**, *2* (9), 628–636. https://doi.org/10.1038/35023579.

(19) Sellers, K. J.; Elliott, C.; Jackson, J.; Ghosh, A.; Ribe, E.; Rojo, A. I.; Jarosz-Griffiths, H. H.; Watson, I. A.; Xia, W.; Semenov, M.; Morin, P.; Hooper, N. M.; Porter, R.; Preston, J.; Al-Shawi, R.; Baillie, G.; Lovestone, S.; Cuadrado, A.; Harte, M.; Simons, P.; Srivastava, D. P.; Killick, R. Amyloid β Synaptotoxicity Is Wnt-PCP Dependent and Blocked by Fasudil. *Alzheimer's Dement.* **2018**, *14* (3), 306–317. https://doi.org/10.1016/J.JALZ.2017.09.008.

(20) Cichon, J.; Sun, C.; Chen, B.; Jiang, M.; Chen, X. A.; Sun, Y.; Wang, Y.; Chen, G. Cofilin Aggregation Blocks Intracellular Trafficking and Induces Synaptic Loss in Hippocampal Neurons. *J. Biol. Chem.* **2012**, *287* (6), 3919. https://doi.org/10.1074/JBC.M111.301911.

(21)   Pozueta, J.; Lefort, R.; Shelanski, M. L. Synaptic Changes in Alzheimer's Disease and Its Models. *Neuroscience* **2013**, *251*, 51–65. https://doi.org/10.1016/J.NEUROSCIENCE.2012.05.050.

(22)   Kudryashov, D. S.; Reisler, E. ATP and ADP Actin States. *Biopolymers* **2013**, *99* (4), 245–256. https://doi.org/10.1002/bip.22155.

(23)   Wioland, H.; Guichard, B.; Senju, Y.; Myram, S.; Lappalainen, P.; Jégou, A.; Romet-Lemonne, G. ADF/Cofilin Accelerates Actin Dynamics by Severing Filaments and Promoting Their Depolymerization at Both Ends. *Curr. Biol.* **2017**, *27* (13), 1956-1967.e7. https://doi.org/10.1016/j.cub.2017.05.048.

(24)   Carlier, M.-F.; Laurent, V.; Santolini, J.; Melki, R.; Didry, D.; Xia, G.-X.; Hong, Y.; Chua, N.-H.; Pantaloni, D. Actin Depolymerizing Factor (ADF/Cofilin) Enhances the Rate of Filament Turnover: Implication in Actin-Based Motility. *J. Cell Biol.* **1997**, *136* (6), 1307. https://doi.org/10.1083/JCB.136.6.1307.

(25)   Salem, F. B.; Bunner, W. P.; Prabhu, V. V; Kuyateh, A.-B.; O'Bryant, C. T.; Murashov, A. K.; Szatmari, E. M.; Hughes, R. M. CofActor: A Light- and Stress-Gated Optogenetic Clustering Tool to Study Disease-Associated Cytoskeletal Dynamics in Living Cells. *J. Biol. Chem.* **2020**, jbc.RA119.012427. https://doi.org/10.1074/jbc.ra119.012427.

(26)   Tanaka, K.; Takeda, S.; Mitsuoka, K.; Oda, T.; Kimura-Sakiyama, C.; Maéda, Y.; Narita, A. Structural Basis for Cofilin Binding and Actin Filament Disassembly. *Nat. Commun.* **2018**, *9* (1), 1860. https://doi.org/10.1038/s41467-018-04290-w.

(27)   Lehenkari, P. P.; Kellinsalmi, M.; Näpänkangas, J. P.; Ylitalo, K. V; Mönkkönen, J.; Rogers, M. J.; Azhayev, A.; Väänänen, H. K.; Hassinen, I. E. Further Insight into Mechanism of Action of Clodronate: Inhibition of Mitochondrial ADP/ATP Translocase by a Nonhydrolyzable, Adenine-Containing Metabolite. *Mol. Pharmacol.* **2002**, *61* (5), 1255–1262. https://doi.org/10.1124/mol.61.5.1255.

(28)   Lecka, J.; Ben-David, G.; Simhaev, L.; Eliahu, S.; Oscar, J.; Luyindula, P.; Pelletier, J.; Fischer, B.; Senderowitz, H.; Sévigny, J. Nonhydrolyzable ATP Analogues as Selective Inhibitors of Human NPP1: A Combined Computational/Experimental Study. *J. Med. Chem.* **2013**, *56* (21), 8308–8320. https://doi.org/10.1021/jm400918s.

(29)   Bhattacharya, S.; Verrill, D. S.; Carbone, K. M.; Brown, S.; Yule, D. I.; Giovannucci, D. R. Distinct Contributions by Ionotropic Purinoceptor Subtypes to ATP-Evoked Calcium Signals in Mouse Parotid Acinar Cells. *J. Physiol.* **2012**, *590* (11), 2721–2737. https://doi.org/10.1113/jphysiol.2012.228148.

(30)   Weisman, G. A.; Ajit, D.; Garrad, R.; Peterson, T. S.; Woods, L. T.; Thebeau, C.; Camden, J. M.; Erb, L. Neuroprotective Roles of the P2Y2 Receptor. *Purinergic Signal.* **2012**, *8* (3), 559. https://doi.org/10.1007/S11302-012-9307-6.

(31)   McLarnon, J. G.; Ryu, J. K.; Walker, D. G.; Choi, H. B. Upregulated Expression of Purinergic P2X7 Receptor in Alzheimer Disease and Amyloid-β Peptide-Treated

Microglia and in Peptide-Injected Rat Hippocampus. *J. Neuropathol. Exp. Neurol.* **2006**, *65* (11), 1090–1097. https://doi.org/10.1097/01.JNEN.0000240470.97295.D3.

(32)   T, T.; K, S.; A, S.; M, F.; M, W.; S, S.; Y, I.; H, K.; M, H. P2X7 Receptor Signaling Pathway as a Therapeutic Target for Neurodegenerative Diseases. *Arch. Immunol. Ther. Exp. (Warsz).* **2010**, *58* (2), 91–96. https://doi.org/10.1007/S00005-010-0069-Y.

(33)   Cieślak, M.; Wojtczak, A. Role of Purinergic Receptors in the Alzheimer's Disease. *Purinergic Signal.* **2018**, *14* (4), 331–344. https://doi.org/10.1007/s11302-018-9629-0.

(34)   RCSB PDB - 1Q8G: NMR structure of human Cofilin https://www.rcsb.org/structure/1Q8G (accessed Jul 26, 2021).

(35)   Reporter Genes & Expression Vectors for Transient Transfection http://www.genlantis.com/phcmv-fusion-stable-reporter-vectors.html (accessed Jul 22, 2021).

(36)   Riedl, J.; Crevenna, A. H.; Kessenbrock, K.; Yu, J. H.; Neukirchen, D.; Bista, M.; Bradke, F.; Jenne, D.; Holak, T. A.; Werb, Z.; Sixt, M.; Wedlich-Soldner, R. Lifeact: A Versatile Marker to Visualize F-Actin. *Nat. Methods* **2008**, *5* (7), 605. https://doi.org/10.1038/NMETH.1220.

(37)   Belyy, A.; Merino, F.; Sitsel, O.; Raunser, S. Structure of the Lifeact–F-Actin Complex. *bioRxiv* **2020**, 2020.02.16.951269. https://doi.org/10.1101/2020.02.16.951269.

(38)   Flores, L. R.; Keeling, M. C.; Zhang, X.; Sliogeryte, K.; Gavara, N. Lifeact-GFP Alters F-Actin Organization, Cellular Morphology and Biophysical Behaviour. *Sci. Rep.* **2019**, *9* (1), 1–13. https://doi.org/10.1038/s41598-019-40092-w.

(39)   Courtemanche, N.; Pollard, T. D.; Chen, Q. Avoiding Artefacts When Counting Polymerized Actin in Live Cells with LifeAct Fused to Fluorescent Proteins. *Nat. Cell Biol. 2016 186* **2016**, *18* (6), 676–683. https://doi.org/10.1038/ncb3351.

(40)   Yang, L.; Wang, X.; Deng, W.; Mo, W.; Gao, J.; Liu, Q.; Zhang, C.; Wang, Q.; Lin, C.; Zuo, Z. Using HEK293T Expression System to Study Photoactive Plant Cryptochromes. *Front. Plant Sci.* **2016**, *7*, 940. https://doi.org/10.3389/fpls.2016.00940.

(41)   Millet, J. K.; Tang, T.; Nathan, L.; Jaimes, J. A.; Hsu, H. L.; Daniel, S.; Whittaker, G. R. Production of Pseudotyped Particles to Study Highly Pathogenic Coronaviruses in a Biosafety Level 2 Setting. *J. Vis. Exp.* **2019**, *2019* (145). https://doi.org/10.3791/59010.

(42)   Jarvis, M. F.; Khakh, B. S. ATP-Gated P2X Cation-Channels. *Neuropharmacology* **2009**, *56* (1), 208–215. https://doi.org/10.1016/J.NEUROPHARM.2008.06.067.

(43)   Chen, C. K.; Benchaar, S. A.; Phan, M.; Grintsevich, E. E.; Loo, R. R. O.; Loo, J. A.; Reisler, E. Cofilin-Induced Changes in F-Actin Detected via Cross-Linking with Benzophenone-4-Maleimide. **2013**. https://doi.org/10.1021/bi400715z.

(44)   Ishikawa-Ankerhold, H. C.; Ankerhold, R.; Drummen, G. P. C. Advanced Fluorescence
         Microscopy Techniques—FRAP, FLIP, FLAP, FRET and FLIM. *Molecules* **2012**, *17* (4),
         4047. https://doi.org/10.3390/MOLECULES17044047.

(45)   Toshima, J.; Toshima, J. Y.; Amano, T.; Yang, N.; Narumiya, S.; Mizuno, K. Cofilin
         Phosphorylation by Protein Kinase Testicular Protein Kinase 1 and Its Role in Integrin-
         Mediated Actin Reorganization and Focal Adhesion Formation. *Mol. Biol. Cell* **2001**, *12*
         (4), 1131. https://doi.org/10.1091/MBC.12.4.1131.

(46)   Kim, J.-S.; Huang, T. Y.; Bokoch, G. M. Reactive Oxygen Species Regulate a Slingshot-
         Cofilin Activation Pathway. *Mol. Biol. Cell* **2009**, *20* (11), 2650.
         https://doi.org/10.1091/MBC.E09-02-0131.

(47)   Sprague, B. L.; Pego, R. L.; Stavreva, D. A.; McNally, J. G. Analysis of Binding
         Reactions by Fluorescence Recovery after Photobleaching. *Biophys. J.* **2004**, *86* (6), 3473.
         https://doi.org/10.1529/BIOPHYSJ.103.026765.